Joint Inversion of SPREE Receiver Functions and Surface Wave Dispersion Curves for 3-D Crustal and Upper Mantle Structure Beneath the U.S. Midcontinent Rift

G. I. Aleqabi[1], M. E. Wysession[1], D. A. Wiens[1], W. Shen[2], S. Van der Lee[3], F. A. Darbyshire[4], A. W. Frederiksen[5], S. Stein[3], D. Jurdy[3], and J. Revenaugh[6]

[1]Department of Earth and Planetary Sciences, Washington University in St. Louis, St. Louis, MO, USA
[2]Department of Geosciences, Stony Brook University, Stony Brook, NY, USA
[3]Department of Earth and Planetary Science, Northwestern University, Evanston, IL, USA
[4]Centre de recherche GEOTOP, Université du Québec à Montréal, Montreal, Quebec, Canada
[5]Department of Earth Sciences, University of Manitoba, Manitoba, Canada
[6]Department of Earth Sciences, University of Minnesota, Twin Cities, Minneapolis, MN, USA

Corresponding author: Michael Wysession (mwysession@wustl.edu)

Key Points:

- The crustal depth increases to at least 50 km beneath the Mid-Continent Rift (MCR) of Wisconsin (WI) and Minnesota (MN).
- The Moho beneath the WI/MN MCR contains a thick layer 40-60 km deep (Vs = 4.1-4.6 km/s) that may be underplated mafic volcanic material.
- Beneath the WI/MN MCR, Vs is generally slower than average in the upper crust but faster than average in the lower crust / upper mantle.

Abstract

Broadband seismograms from the EarthScope Transportable Array and Superior Province Rifting EarthScope Experiment (SPREE) deployments are used to map the crust and uppermost mantle structures beneath the failed Midcontinent Rift (MCR) of Minnesota/Wisconsin, USA. The results suggest the existence of a variable zone of mafic underplating that is up to 20 km thick (40-60 deep). We jointly invert receiver functions and Rayleigh wave dispersion curves to quantify the region's crustal and mantle shear-wave velocity structure. Basin sediment thicknesses are mildly asymmetric about the rift axis, with thickest regions immediately beneath the rift. 3-D modeling shows anomalous lower crust and crust-mantle transitions beneath the MCR. Sub-MCR crustal thicknesses are generally >50 km with lower crust Vs of 4.0-4.2 km/s. Away from the MCR, the crust is typically ~40 km thick. Strong variations in apparent crustal thickness are found along the MCR, increasing significantly in places. An additional layer of shear velocities intermediate between typical lower crust and upper mantle velocities (4.1-4.6 km/s) exists beneath most of the MCR which is thickest beneath the rift axis and pinches out away from the rift. This structure corroborates previous proposals of the presence of an underplated layer near the Moho. Results cannot distinguish between different mechanisms of emplacement (e.g., mafic interfingering within a subsequently down-dropped lower crust vs. development of a high-density pyroxenitic residuum at the top of the mantle). Also observed are anomalously high (>4.7 km/s) sub-rift shear-wave velocities at ~70-90-km depths, suggesting the presence of cold, depleted upper mantle material.

Plain Language Summary

The Mid-Continent Rift is a failed continental rift that nearly split North America into two continental fragments 1.1 billion years ago. Unlike typical continental rift zones, which are characterized by stretched, thinned, and normal-faulted crust, the base of the mantle beneath the Mid-Continent Rift sits more than 10 km below the surrounding regions and has shown evidence of being infilled by a thick layer of erupted volcanic basalt that may be 15-20 km thick in places. In addition, the base of the crust beneath the rift appears to contain an underplated layer of mafic volcanic materials that is itself 15-20 km thick in places, extending to depths of up to 60 km. The unique nature of this tectonic event left significant alterations to the lithosphere of North America that retain a strong seismic signature, even 1.1 billion years after the event.

1 Introduction

The Superior Province Rifting EarthScope Experiment (SPREE, Figure 1; Van der Lee et al., 2011) was designed to study the seismic structure of the crust and mantle lithosphere of the Midcontinent Rift of North America (MCR) using several seismic methods including receiver function analysis and surface wave tomography. Our study area includes the southern part of the Archean Superior Craton (Canadian Shield) and the Paleoproterozoic Yavapai and Penokean orogenic belts to its south. Cross-cutting these terranes is the Mesoproterozoic Midcontinent Rift system (e.g., Morgan, 1971; Green, 1983; Stein et al., 2015). The region's complex tectonics are shown in Figure 2.

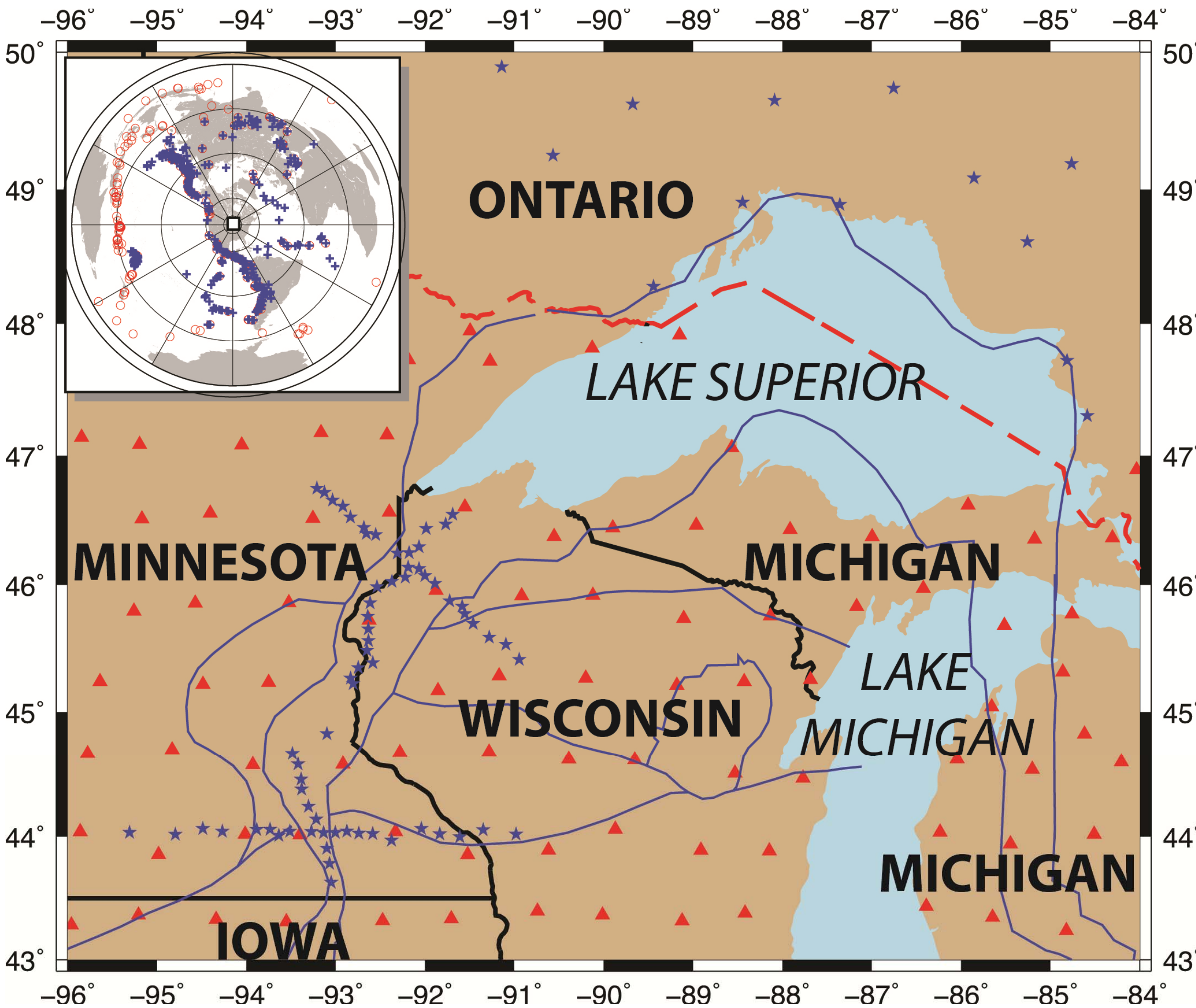

Figure 1. Study area, showing locations of the Superior Rifting EarthScope Experiment (SPREE) stations (blue asterisks) and Transportable Array stations (red triangles). Blue lines are boundaries of the Mid-Continent Rift and other tectonic domains, which are defined and referenced in the caption to Figure 2. Light blue areas are lakes. Black lines are state boundaries and the red dashed line is the U.S. – Canada border. The upper left inset shows the locations of earthquakes used for calculating P-wave receiver functions (red circles) and surface wave dispersion measurements (blue crosses). The inset concentric circles represent distances from the SPREE array in increments of 25°.

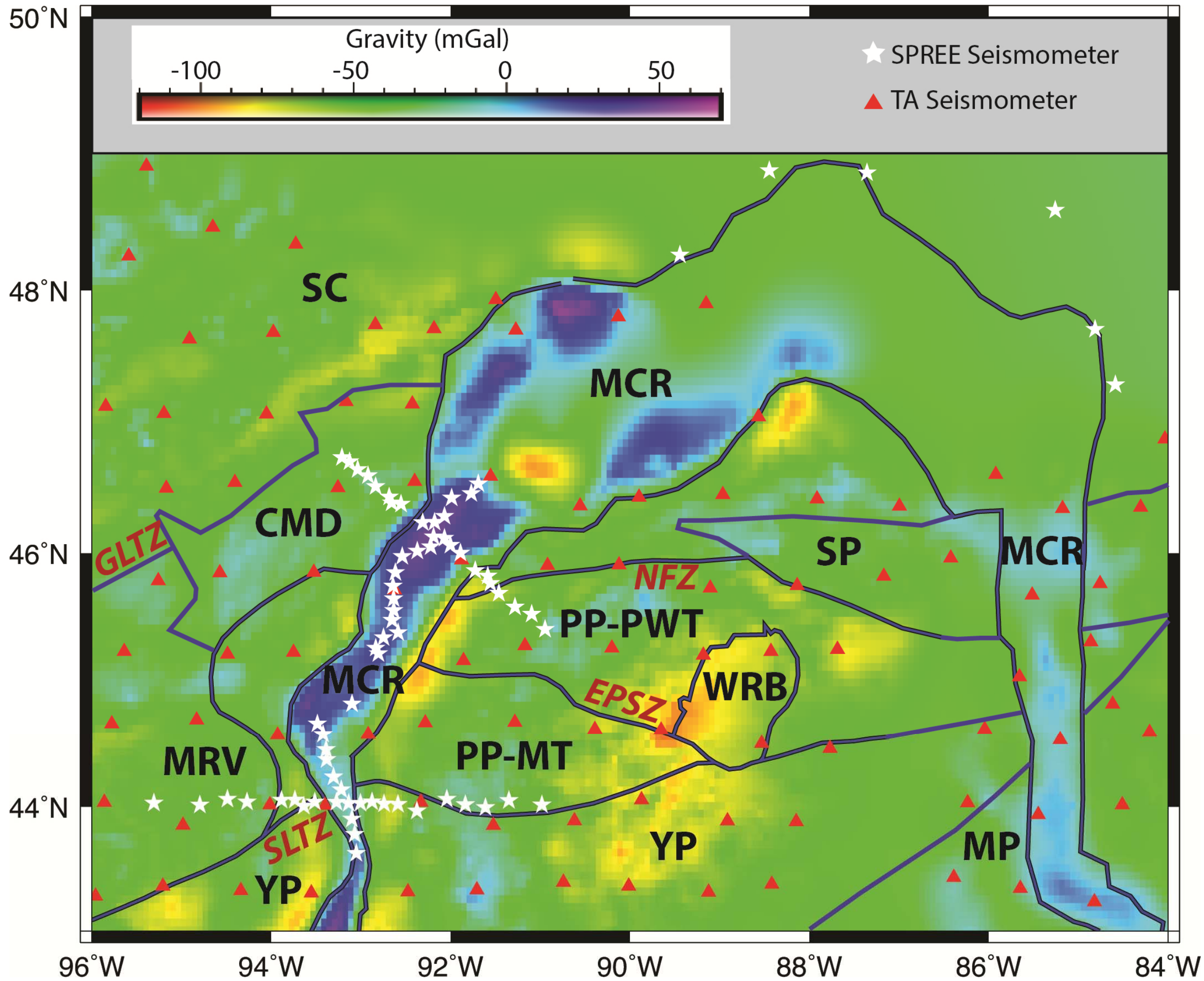

Figure 2. Tectonic map of the north-central United States showing the distribution of Precambrian terranes in the vicinity of the Mid-Continent Rift (MCR) (from Holm et al., 2007; Whitmeyer and Karlstrom, 2007; Rivers, 2015): CMD = Craton-Margin Domain, EPSZ = Eau Pleine Shear Zone, GLTZ = Great Lakes Tectonic Zone, MP = Mazatlal Province, MRV = Minnesota River Valley, NFZ = Niagara Fault Zone, PP-MT = Marshfield Terrance of the Penokean Province, PP-PWT = Pembine-Wausau Terrance of the Penokean Province, SC = Superior Craton, SLTZ = Spirit Lake Tectonic Zone, SP = Southern Province, and YP = Yavapai Province. Shaded colors are Bouguer gravity anomalies, with blue/purple showing positive anomalies and green/yellow/red showing negative anomalies (Aldouri and Keller, 2011). This data set only extends to a latitude of 49°. The MCR axis generally shows high positive Bouguer gravity anomalies. Also shown are SPREE seismic station locations (white asterisks) and TA stations (red triangles).

A large volume of basalt syntectonically filled parts of the MCR, though its origin is unknown. A mantle plume hypothesis has been used to explain the existence of the flood basalts in the rift valley on both sides of the MCR (e.g., Nicholson et al., 1997; Hutchinson et al., 1990; Davis et al., 2022; Prasanna et al., 2022), although the lack of significant topographic relief has been used to argue against this (Campbell, 2001).

Stein et al. (2018) explain the development of the MCR as a result of deformational processes during a reorganization of plate motions and the resulting evolution of plate margins, suggesting that deformation caused decompression melting and leaky transform faults that resulted in a large volume (up to a million cubic kilometers) of volcanic basalt. This model explains the asymmetric gravity anomaly and volcanic volumes of the MCR (Merino et al., 2013; Elling et al., 2022) as a consequence of the east and west arms being boundaries between a microplate and two diverging major plates. The MCR's intersection with the Superior Craton is a defining area within which to study rift inception and demise.

An alternative explanation of the development of the MCR is presented by Swanson-Hysell et al. (2023), who connect prolonged subduction of oceanic lithosphere beneath southeast Laurentia in the Mesoproterozoic with the initiation of voluminous mafic magmatism of the MCR via a deep mantle water cycle. They proposed that dense hydrous minerals subducted to the bottom of the upper mantle before dehydrating and initiating upwelling, decompression melting, and intraplate magmatism. Subsequent collisional orogenic events, including the Grenvillian orogeny, combined multiple Proterozoic terranes into the supercontinent Rodinia, and these associated with the cessation of the rifting of the MCR.

The SPREE seismic deployment was designed to identify any crustal modifications across the MCR and to resolve the surrounding mantle structure. A goal of SPREE was to determine the role of the mantle in this major 1.1-billion-year-old rifting event and in the subsequent evolution of the dormant and deep MCR. In this study we present crustal thickness and shear velocity variations (Vs) obtained for the MCR from a joint inversion of receiver functions and surface waves.

Numerous geophysical studies (e.g., Van Schmus, 1992; Miller and Nicholson, 2013; Foster et al., 2020) have examined the MCR by quantifying the contrast between the rift valley and its surroundings. This contrast is seen in the composition, gravity, and magnetic signatures of the crust and mantle (Van Schmus & Hinze, 1985; Stein et al., 2014, 2018; Zhang et al., 2016; Elling et al., 2022). The prominent gravity anomalies shown in Figure 2 define the geographic extent of the MCR (Chandler & Lively, 2011). Volcanism formed dense basalt and gabbro deposits in the rift, which subsided and was filled by non-volcanic sediments. Subsequent compression uplifted the rift interior (Cannon et al., 1989; Stein et al., 2018). Although previous seismological research has provided significant information about the MCR, the nature of the crust and upper mantle velocity structures remains undetermined.

The resistivity structure of the MCR was explored using data from the long period EarthScope magnetotelluric (MT) transportable array. The resulting three-dimensional inversion shows that the western arm has a highly resistive core straddled by conductive basins that consist of two deep-seated east-west-trending anomalous changes. These MT features coincide with two surface-mapped sutures, the Spirit Lake tectonic zone and the Niagara Fault (Yang et al., 2015) (Figure 2). Merino et al. (2013) modeled gravity data collected across the two arms and found significant variations in the inferred volume of volcanics. The basalt volume seems to increase toward the Lake Superior region, with more magmatism within the western arm compared to the eastern arm, although the increased uplift of the western limb, when compared to the eastern limb, also affects the gravity signature.

Active-source seismic studies in the region, notably the 1986 Great Lakes International Multidisciplinary Program on Crustal Evolution (GLIMPCE) reflection profiles across the MCR in Lakes Superior and Michigan show the rift basin to be very wide there. The southern edge of the basin seems to be bounded by a normal growth fault and flat-lying clastic layers with a total thickness of 12-14 km, with the Moho characterized by a reflection time of more than 11 s (Behrendt et al., 1988). Using GLIMPCE data, large crustal thickening was identified beneath the Lake Superior part of the MCR, where the crustal thickness reaches 55 km (Shay & Trehu, 1993; Hamilton & Mereu, 1993). The high-velocity, high-density bottom 20 km of the crust were interpreted as a “volcanic root” of mafic material added to the bottom of the crust during rifting (Tréhu et al., 1991).

The MCR crustal structure in central Iowa was previously analyzed using receiver functions (e.g., French et al., 2009; Moidaki et al., 2013) from the Florida-to-Edmonton Broadband Seismometer Array data (Wysession & Fischer, 2001). Moidaki et al. (2013) found anomalously thick crust in the Iowa segment of the MCR, in comparison with the surrounding regions. Shen et al. (2013b) found anomalously thick crust beneath the western arm. They also observed that the Moho was sharp beneath the southern part of the MCR but was gradually transitional in the northern part.

Zhang et al. (2016), using a P-wave receiver function analysis of teleseismic SPREE and TA seismic data, concluded that the Moho in the area surrounding Lake Superior and away from the rift zone is relatively flat with an average depth of 40 km. In addition, they found that the entire portion of the western MCR arm that was sampled by SPREE is underlain by a similar sub-crustal mafic layer as found beneath Lake Superior, with a thickness between 10 and 15 km that formed from crustal underplating during rifting. Pollitz and Mooney (2016), using TA surface waves to study the crustal and shallow upper mantle of Central United States, proposed that thermal lithospheric disturbances can have a lingering effect by lowering seismic velocities for long periods of time, suggesting that low seismic velocities at depths of about 15 km are associated with failed rift systems, which are often coincident with shallow sedimentary basins.

Foster et al. (2020) used anisotropic Rayleigh wave tomography to study crust and upper mantle structure across northern Ontario (Canada), the MCRZ and the Proterozoic terranes of the central-northern USA. The resulting phase velocity maps showed systematic differences between the (seismically fastest) Superior craton and the (relatively slower) Proterozoic domains. Superimposed on this trend was an arcuate low-velocity feature, most prominent at periods <80 seconds (depths of <120 km) whose position matched the outline of the MCRZ. This feature was also correlated with a change in orientation and amplitude of azimuthal anisotropy. Boyd and Smithson (1993) found that the gneissic crustal terrane beneath the Minnesota River Valley sub-province had an average P-wave velocity of 6.8 km/s and thickness of 49 km, deeper than the surrounding crust's thicknesses of 35–40 km.

Here, seismic records from the SPREE and EarthScope TA seismic stations are analyzed utilizing two seismic methods: (1) ambient noise tomography, in the style of Barmin et al. (2001), Bensen et al. (2007), Yang et al. (2007), and Lin et al. (2008); and (2) the Automated Surface Wave Measuring System (ASWMS) method for analyzing Rayleigh waves, developed by Jin and Gaherty (2015). Rayleigh surface wave dispersion measurements from both ambient noise and ASWMS are combined with receiver functions and jointly inverted using a Bayesian

Monte Carlo formalism developed by Shen et al. (2013a,b,c). The addition of receiver functions has the benefit of improving the crustal thickness estimation (Shen et al., 2018), due to their sensitivity to seismic discontinuities.

The inversion scheme consists of first using the ambient noise and ASWMS results to invert for 2-D maps of surface wave phase and group velocities and then inverting for the 3-D spatial shear-velocity structure. First, a series of 2-D phase or group velocity maps for different periods are estimated using tomographic methods. At discrete 0.5-degree intervals of latitude and longitude, group and phase velocities at discrete periods are obtained, creating a set of 1-D dispersion curves. These curves are combined with receiver functions at SPREE and TA stations and inverted for 1-D vertical shear-velocity profiles beneath each location in the manner of Shen et al. (2013b). The 1-D shear velocity profiles are then interpolated to construct a continuous 3-D model, providing the basis for geologic interpretations.

The goal of this approach, combining the surface waves and receiver functions, is to provide a higher degree of resolution in imaging the structure, particularly the deep structure, of one of the more enigmatic Precambrian tectonic features of the globe. As pointed out, significant debates still occur as to the cause, mechanism, and process of the formation of the MCR. Although the once-significant thermal anomalies associated with the rift formation are now gone, the hope is that there are remnant compositional features that are still seismically observable and can provide constraints on the dynamic petrochemical processes involved. Receiver functions are particularly good at identifying horizontal discontinuous boundaries, with good vertical resolution, but can’t say much about gradual changes in seismic velocities and have very limited lateral resolution. Surface waves do provide information about continuous vertical gradients in seismic velocity and their inversion can provide reasonable horizontal variations, but their resolution is limited to intermediate wavelengths and they do not do a good job resolving discontinuities. Inverting the surface waves with the receiver functions achieves a greater resolution that is able to resolve features such as a subcrustal underplated layer, limited in both vertical and horizontal extent.

2 Geologic Setting and Tectonic History of the Mid-Continent Rift

An overview of the tectonic history of the MCR, including its overprint on the Archean Superior Province is given by Holm et al. (2007). The MCR cuts through a lithosphere composed of numerous older accreted Archean and Proterozoic terranes (Figure 2). The oldest rocks found in the region (present-day Minnesota and NW Ontario) are those of the southern Superior Province, the world's largest and best-preserved Archean craton. Separate continental and oceanic belts, the Wabigoon, Quetico, Wawa-Abitibi and Minnesota River Valley terranes, were amalgamated by 2.6 Ga during the final cratonization process (e.g., Percival et al., 2012; Jirsa et al., 2011).

Later in the Paleoproterozoic (1850 Ma), the 200-km-wide Penokean Orogeny formed along the southern margin of the Archean Superior craton, a result of continental collision (e.g., Whitmeyer and Karlstrom, 2007). During the Penokean Orogeny, south of the Niagara fault (the boundary between the Penokean Province and the Archean Superior margin, as shown in Figure 2), the Pembine-Wausau oceanic arc was amalgamated onto the southern margin of the Archean Superior craton. Later, near the end of the Penokean orogeny, the Marshfield terrane was accreted onto the Pembine-Wausau Terranes (Schulz & Cannon, 2007). The Penokean crust in Minnesota contains highly deformed metamorphic and plutonic rocks that formed during the Yavapai and Mazatzal orogenies (Jirsa et al., 2011). South of the Penokean province, imprinted on the Mazatlal basement, the rocks of the eastern and southern Granite-Rhyolite Provinces (1340-1400 Ma) and the Central Plains province were emplaced (1600-1800 Ma) (Van Schmus et al., 1987; Sims et al., 1989).

During the Mesoproterozoic (1.1 Ga), the MCR formed by crustal extension marked by episodes of intensive magmatic upwelling. The outstretched arms of the MCR are filled with flood basalts and magmatic intrusions that are 10-25 km thick (Miller and Nicholson, 2013; Stein et al., 2018), covered by clastic rocks that later accumulated within the rift grabens (Chandler et al., 1989). Magnetic and gravitational potential field studies identify large anomalies associated with the MCR. The gravity and magnetic highs (Figure 2) indicate layers of dense and predominantly mafic volcanic rocks flanked and overlain by nearly flat-lying younger sedimentary rocks. After uplift of the central portion of the rift and associated erosion of these sedimentary rocks along the rift axis, the remaining marginal sedimentary rocks have relatively low densities and are essentially non-magnetic, therefore negative gravity anomalies and subdued magnetic signatures usually flank the strongly positive signatures (Allen et al., 1997; Chandler et al., 1989; Elling et al., 2022).

Two competing mechanisms attempt to explain the formation of the MCR. Many igneous features of the MCR, such as melting of an upwelling enriched mantle and the emplacement of an enormous volume of relatively homogeneous magma within a restricted time interval, suggest that a hot plume was either responsible for the inception of the rifting (e.g., Nicholson et al., 1997; White, 1997; Vervoort et al., 2007) or influenced the location of the rifting during the period of continental extension that resulted from the Laurentia-Amazonia rifting to the southeast (Stein et al., 2014).

The competing hypothesis suggests that the dynamics of the Grenvillian Orogeny, with the Grenville Province accreted onto the southeastern border of the North American craton, caused the growth of the MCR (Gordon & Hempton, 1986; Cambray & Fujita, 1991). In this mechanism, the MCR evolved out of the strike-slip faults that formed in either the foreland and hinterland of the Grenvillian orogenic zones. Supporters of this mechanism contest the notion of a mantle plume by noting the observed lack of a large pre-volcanism uplift that would have resulted from the thermal anomaly of a plume head rising beneath the mid-continental lithosphere (Campbell, 2001).

Several lines of data support the magmatic influence of a mantle plume. Gravity data support the magmatic underplating of the lower crust of the MCR beneath Lake Superior (Behrendt et al., 1988; Hutchinson et al., 1990; Thomas & Teskey, 1994), possibly facilitated by an anomalously hot mantle plume (Hutchinson et al., 1990; Davis and Green, 1997). Isotopic data from exposed mafic rocks within the MCR display Nd and Pb isotopic compositions that indicate being derived from a homogeneous, isotopically enriched mantle plume (Nicholson & Shirey, 1990; Shirey et al., 1994; Nicholson et al., 1997). Miller & Nicholson (2013) proposed that an anomalously hot mantle plume removed a portion the Proterozoic crust and built an extensional rift zone with the emplacement of a large volume of mineral-rich volcanics. Van der Pluijm & Marshak (2004) suggested that heat from the plume caused partial melting through asthenospheric decompression, producing a great volume of hot, low-viscosity magma that led to extensive thermal and igneous activity, one of the thickest sequences of igneous rocks in the world. The complete rift contains an estimated 2.0×10^6 km^3 of igneous material, mainly tholeiitic flood basalts, with an equivalent amount of intrusive underplated material beneath the rift (Ojakangas et al., 2001; Zhang et al., 2016; Stein et al., 2018).

Compilation of U-Pb zircon dating of volcanic igneous rocks from various areas along the MCRZ identified phases of magmatic evolution accompanied by two normal and two reverse magnetic polarities (Middleton et al., 2004). The MCR magmatism continued for 23 My, during the period from 1109 to 1086 Ma (Ojakangas et al., 2001). Miller and Nicholson (2013) detailed six stages of magmatism and tectonism during 1115-1040 Ma involving plume-induced magmatism, crustal underplating, thermal collapse of the plume, and a transition to compressional stresses across the rift system.

Following the cessation of volcanism, spreading ceased across the MCR and an ocean basin never formed. Eventually compression, likely related to the Grenvillian Orogeny, inverted the graben-bounding normal faults into reverse faults. This compression caused about 30 km of horizontal crustal shortening across the MCR (Cannon et al., 1991; Cannon, 1994).

Crustal thicknesses along the MCR varied both temporally and spatially. During the early doming period, Allen et al. (1995) estimated that the crust was locally thinned to roughly a third of its original thickness, based on migrated seismic reflection profiles. Later volcanic episodes thickened the rift by about 20 km, causing both the density and seismic velocity of the underplated lower crust to increase in response to the mantle-derived intrusions and crustal underplating (Stein et al., 2015). Eventually these sequences were followed by the deposition of about 10 km of post-volcanic clastic sedimentary strata (Dickas, 1986; Allen et al., 1995; Dickas and Mudrey, 1997). The region has been minimally altered, with the exception of surface geomorphism such as that resulting from glacial activities, over the past billion years.

3 Tomographic Inversion: Data and Methods

3.1 Data

We use seismograms from two temporary deployments of seismometers forming two arrays across and around the MCR (Figure 1). The SPREE Flexible Array (FA, supported by the USArray Array Operations Facility) operated for more than two years between April, 2011, and October, 2013 (Van der Lee et al., 2011; Wolin et al., 2015; Ola et al., 2016; Bollman et al., 2019). The SPREE data set used here consists of 79 broadband seismic stations, with nominal interstation spacing of 30 km, in Minnesota, Wisconsin, and Ontario. The spatial distribution of stations was designed for detailed mapping of the MCR, so distances between stations across and along the rift were shortened. The stations across the MCR form two X-shaped arrays. Of the SPREE stations used in our analyses, 26 are along the strike of the MCRZ, 20 are part of the northern perpendicular line, 20 are part of the southern perpendicular line, and 13 were deployed in Ontario, Canada, north of Lake Superior within the Superior Craton (Figure 2).

The USArray Transportable Array (TA) (IRIS, 2003) was a temporary deployment of seismometers with a nominal spacing of 70 km that traversed the contiguous United States during 2007-2015. TA stations provide data across a much wider region than the SPREE deployment, although at a wider spacing (Figure 1). We used 88 TA stations that were deployed during the time of the SPREE deployment and were within the general region of study.

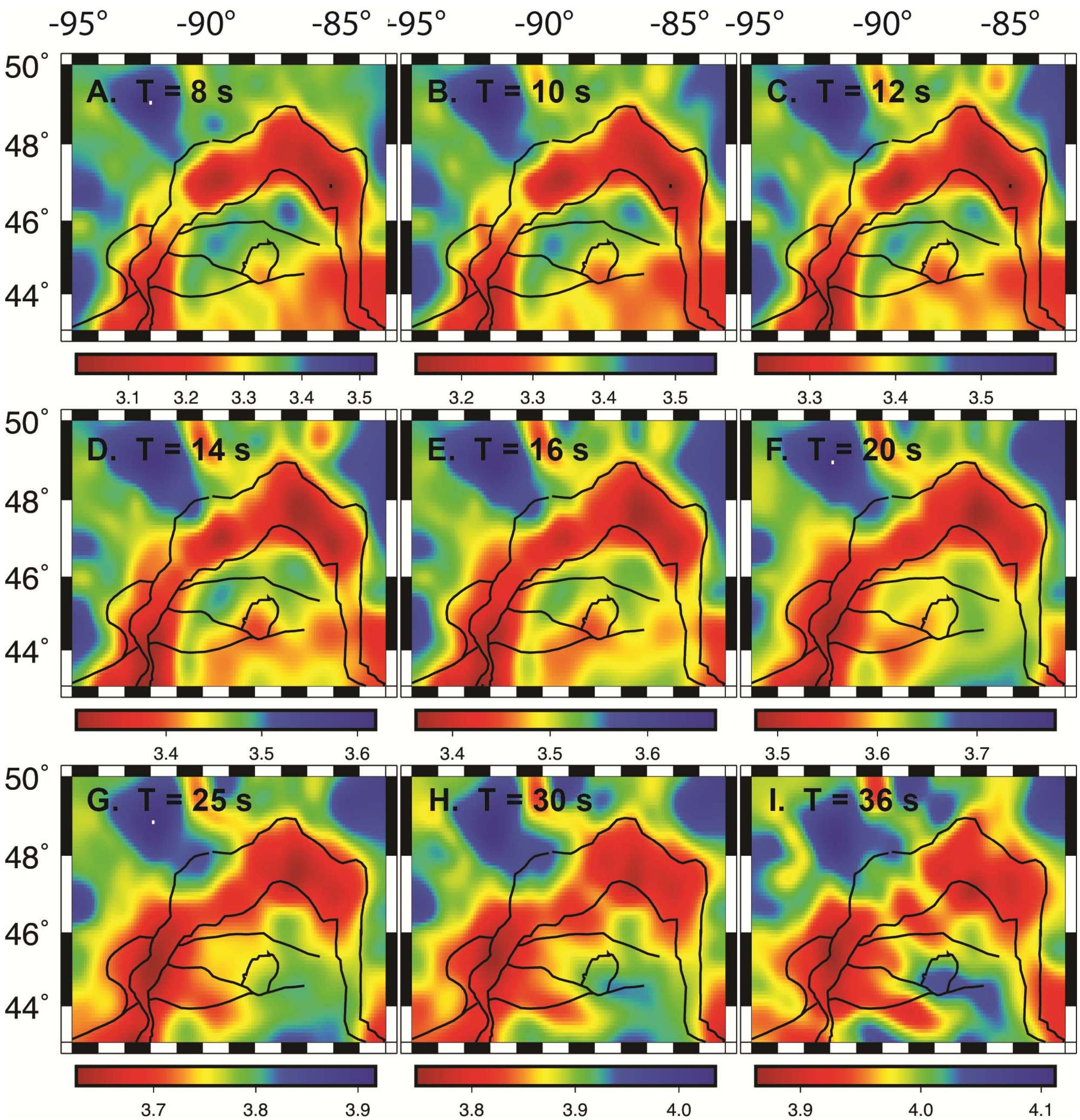

Figure 3. Surface-wave phase velocity maps at periods of 8, 10, 12, 14, 16, 20, 25, 30, and 36 s derived using ambient noise tomography. Black lines show the MCR and other tectonic features as labeled in Figure 2. Note that the velocity scales change for different periods. The MCR shows generally slower phase velocities than surrounding regions.

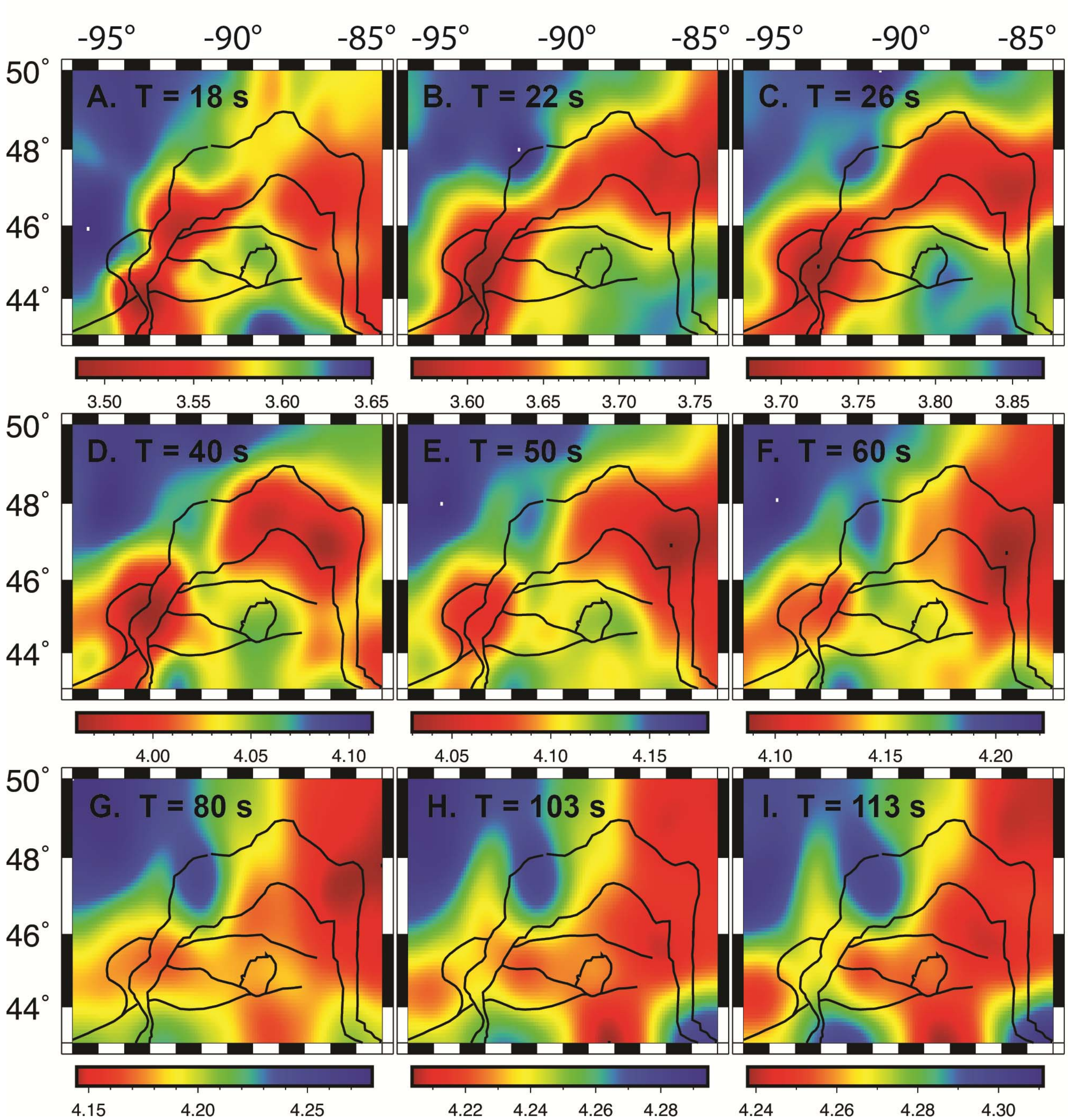

Figure 4. Surface-wave phase velocity maps at periods of 18, 22, 26, 40, 50, 60, 80, 103, and 113 s, derived using the ASWMS method for Rayleigh waves from teleseismic earthquakes. Black lines show the MCR and other tectonic features as labeled in Figure 2. Note that the velocity scales change for the different periods. Similar to Figure 3, the MCR shows generally slower phase velocities at shorter periods (up to T = 60 s), but not at longer periods.

3.2 Surface Wave Methods

Rayleigh wave dispersion was measured using two methods at different period ranges. For shorter periods, between 8 and 36 s, phase and group velocities (Bensen et al., 2007; Yang et al., 2007; Lin et al., 2008) were obtained using ambient noise techniques (phase velocities are shown in Figure 3), and for longer periods we obtained phase velocities using the Automated Surface-Wave Phase-Velocity Measuring System (ASWMS) (Jin and Gaherty, 2015). The locations of the earthquakes used for the interstation surface wave phase velocity measurements were shown as blue crosses in Figure 1.

The ambient noise method is, at this point, well established, using a cross-correlation of long pre-processed time series to create empirical interstation Green's functions. We used time records from April, 2011, through October, 2013, which were initially broken into 1-day segments. Earthquake signals and other known types of interference were removed by time-domain normalization, where the reciprocdal of the mean of the absolute value of the waveform in a moving 80-s time window is used to weight the data value at the center of the window. These weights are determines using a band from 15 s to 50 s, good for identifying earthquakes, but are then applied to the unfiltered data, which are then bandpass filtered between 5 and 100 s. Cross-correlation is then done separately between each pair of stations, and the Rayleigh wave phase velocity dispersion curves are obtained from the symmetric component of each interstation cross-correlogram using an automated frequency-time analysis (Shen et a., 2013b; Benson et al., 2007).

ASWMS is a MATLAB-based package (Jin and Gaherty, 2015) that uses the generalized seismological data functionals of Gee and Jordan (1992), which we used here to obtain phase velocities between 18 and 113 s (Figure 4). We start with broad-band seismograms at one stations containing all seismic phases that may be of interest and use a complementary seismogram from a nearby stations, relative to which all of the phase delays and amplitude anomalies are measured. Cross-corelations are carried out for all station pairs, with any biases between apparent phase velocity and structural phase velocity corrected by adding amplitude measurements into an inversion using an approximation to the Helmholtz equation (Wielandt, 1993; Lin and Ritzwoller, 2011).

Path-dependent dispersion curves were used to provide regional resolution within the tomographic inversion. We applied the tomography technique of Barmin et al. (2001) to obtain tomographic maps of phase and group velocity dispersion for the MCR region. Ambient-noise dispersion measurements from regional records yield the dispersion at periods of less than 20 seconds, which is usually difficult to obtain from either teleseismic or regional earthquakes. For periods longer than 36 s, regional surface-wave tomography maps were obtained using teleseismic earthquakes with the ASWMS Helmholtz tomography method (Jin & Gaherty, 2015). These methods use complementary data sets: the ASWMS method uses only records from earthquakes and the ambient noise method uses the full seismic records minus the earthquake signals.

Phase velocity values at periods in the range of 18 s to 36 s were determined using a combination of both the ambient noise and ASWMS methods. For the overlapping range of periods, we gave preference to the noise results at shorter periods and increasingly shift the preference to the ASWMS values as the period increases. The Monte Carlo method we used requires uncertainty estimates. However, these are not produced by the ambient noise tomographic technique, so we followed the method of Moschetti et al. (2010) and scaled the Rayleigh wave phase uncertainties by the relative errors in the interstation ambient noise dispersion measurements. This resulted in an uncertainty of 0.0217 km/s for the ambient noise results for all periods less than 24 s, which was 50% higher than the value used by Moschetti et al. (2010). At a period of 24 s this scaling provided an uncertainty of 0.0145 km/s (Moschetti et al., 2010), for periods of 24 - 36 s we scaled the uncertainty of 0.0145 according to the period, and for periods above 36 s we chose an uncertainty that was 75% of the average of the reported ASWMS standard deviations across all nodes.

At all periods, for both methods, surface wave phase velocities are generally slower beneath the MCRZ than for regions away from the rift (Figures 3 and 4). These slow phase velocities reflect syn-tectonic and post-tectonic sedimentary clastic rocks in the rift basin. The seismic velocities within the shallow basins are so low that they dominate phase velocities even at longer periods where sensitivities are greater for deeper structures that are anomalously fast. Although inversions of phase and group velocities show that there are indeed depths where seismic velocities are anomalously fast, the phase velocities at periods most sensitive to them (~ 18 - 33 s) still show anomalously low values.

3.3 Receiver Functions

The drawback of surface wave dispersion measurements is their limited sensitivity to sharp velocity contrasts such as the Moho. To remedy this shortcoming, teleseismic Ps receiver functions (RF) from TA and SPREE stations were included in the inversion. The RF computations were performed following the approached described by Shen et al. (2013b,c), which used USArray TA data but not the SPREE data. The receiver functions calculated here used the same algorithms used by Shen et al. (2013b,c) but incorporating both the TA and SPREE data.

This method uses a harmonic-stripping process to reduce the azimuthal dependence of the receiver functions. A harmonic function, $H(\theta, t) = A_0(t) + A_1(t) \sin [\theta + \theta 1(t)] + A_2(t) \sin [2\theta + \theta_2(t)]$, is fit to the azimutally depedent raw receiver functions at each station and at each time t, where A_0 is the azimuthally independent receiver function and A_i (with i = 1,2) are the amplitudes of the harmonic components as a function of the azimuth θ. This procedures approximately removes the azimuthal dependence from receiver functions to retrieve the azimuthally independent receiver function A_0. Dipping crustal interfaces and contamination from azimuthal anisotropy primarily produce signals with π and 2π periodicities (Shen et al. 2013*b*), so this harmonic stripping method produces a reliable estimate of the receiver functions that would have results from a horizontally layered and isotropic medium. Our method of generating receiver functions, as with Shen et al. (2013*b*), uses only *Ps* converted waves, and we select all teleseismic events with $m_b \geq 5.1$ and all stations within a 30° – 90° distance range.

The difference from Shen et al. (2013*b*) is that we have included all of the new data from the SPREE seismic deployment of more than 80 stations. This data set is the same as the one used by the receiver function study of Zhang et al. (2016), which did not incorporate surface waves. Zhang et al. (2016) also used *Ps* conversions, as opposed to some other studies such as Chichester et al. (2018), which used *Sp* conversions, but processed the *Pd* data using a different algorithm. Both our and the Zhang et al. (2016) studies use a time-domain iterative deconvolution method in the manner of Ligorria and Ammon (1999), but Zhang et al. (2016) does not use a harmonic stripping method and uses an H-κ stacking method from Zhu and Kanamori (2000) and a waveform fitting method of Van der Meide et al. (2003). Having the same receiver function data set used and analyzed in different ways provides important scientific reducdancy checks on the geophysical structures revealed, and the similarities and differences between the results are discussion in Section 4.

3.4 Bayesian Monte-Carlo Inversion Method

We carried out simultaneous joint inversions incorporating the three forms of data (phase velocities, group velocities, and receiver functions) using a Bayesian Monte Carlo inversion method. Inversion of surface wave dispersion measurements for a 3-D shear-wave velocity model was carried out in two stages. In the first, tomographic maps obtained by the imaging methods were used to extract local phase and group velocity dispersion curves at grid nodes at the locations of the TA and SPREE stations for which receiver functions were available. In the second stage, we used Monte Carlo methods to infer a 3-D shear-velocity model for the crust and upper mantle structure beneath the MCR and surrounding terranes.

The inversion methods that we used are discussed in Shen et al. (2013a,b,c). For our study, we used a total of 512 nodes, with 167 nodes at the locations of the 79 SPREE stations and 88 TA stations. Group and phase velocities and receiver functions were calculated for each of these nodes. In addition, 345 nodes were established along a rectilinear 23 x 15 grid spanning latitudes of 43°N to 50°N and longitudes of 84.5°W to 95.5°W, with 0.5° increments. Group and phase velocities were identified for each of these grid nodes from the regional tomographic dispersion maps that we calculated using the Barmin et al. (2001) method. The subsequent inversion for velocity structure incorporates the two different sets of nodes, with and without receiver functions. The inversion is carried out independently for each node, with no lateral regularization with surrounding nodes. Figure 5 illustrates the method at one node.

Once the one-dimensional velocity profiles are determined at all of the geographic nodes, the smothed velocity maps are generated using a simple kriging interpolation (Schultz et al., 1999; Shen et al, 2013a). For each depth, at each grid node, we search for stations within a 1-degree radius. The averaged velocity value is determined with a weighting function where the value of each station within the 1-degree radius is weighed according to $[(1 + d_i)\sigma_i]^{-1}$, where d_i is the station-node distance (in degrees) and σ_i is the uncertainty of the model at that depth and station. The results are shown in the following section.

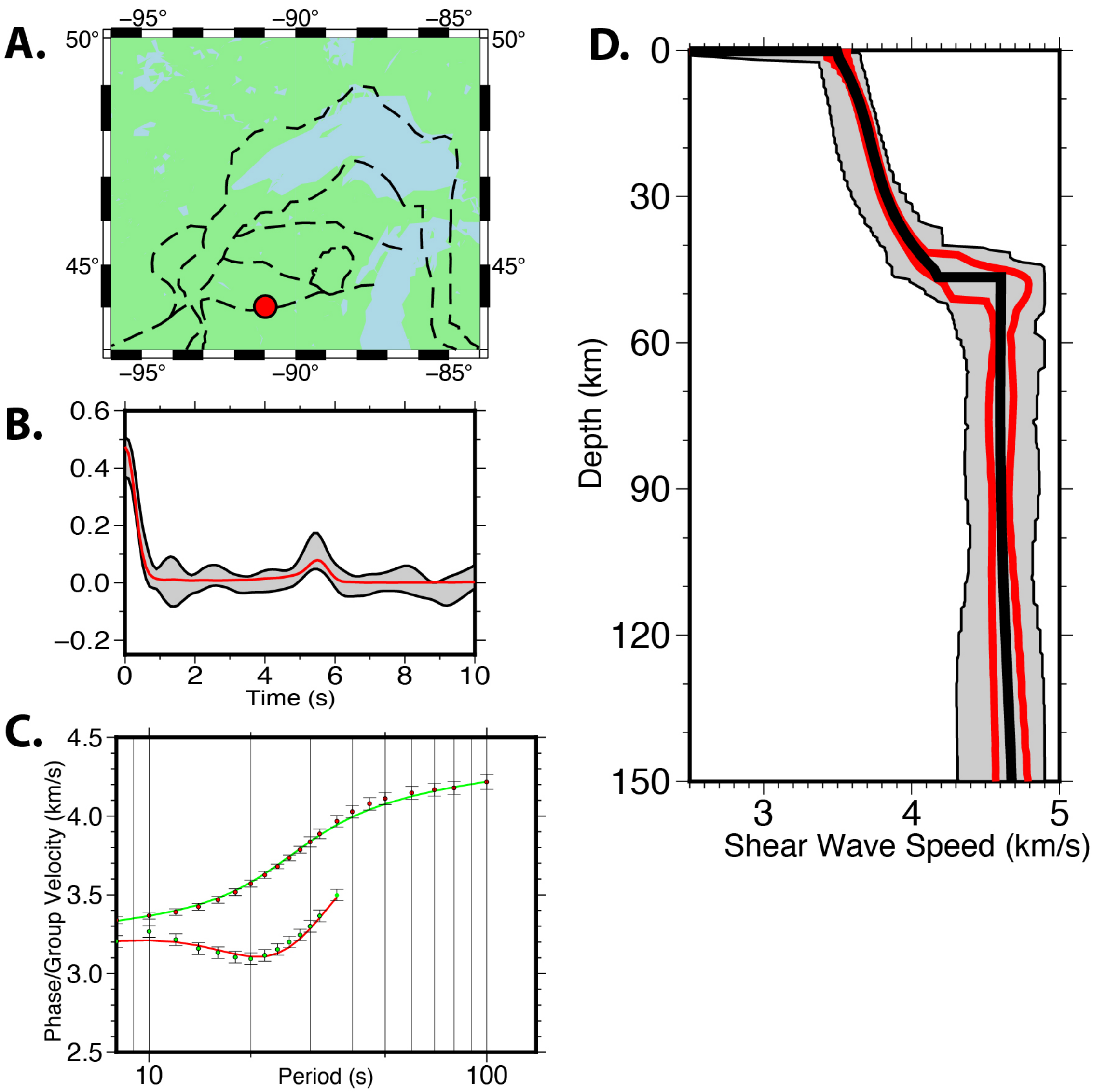

Figure 5. A demonstration of the method used for determining the 1-D vertical velocity structure for a given node. (a) The location of SPREE station SS88 (red circle); (b) The Ps receiver function for that location, with the red line showing the best fit and the shaded gray region showing the 1-σ rms uncertainties; (c) Rayleigh wave phase (green, top) and group (red, bottom) dispersion curves for this node. Group velocities are from the ambient noise method. Phase velocities are obtained through a combination of the ambient noise and ASWMS results using a weighting rubric described in Section 3.2; (d) The resulting vertical shear wave velocity models, with the best model shown by the black line. The red lines show the 1-σ variations and the gray shaded area shows the 2-σ variations of the Monte Carlo results.

4 Results

Figures 6 – 12 show the results of the tomographic inversion. Figure 6 shows shear velocities and standard deviations of the posterior distribution at six depths (horizontal slices) within the crust. Figure 7 shows the resulting crustal thicknesses, represented as Moho depths. Enhanced views of regional variations in crustal thickness and shear velocity are shown for three profiles in Figures 8-12. Figures 8-11 show two profiles, N-N′ and S-S′, that align with the SPREE transects that cross the rift perpendicularly. The locations of these SPREE cross-rift profiles are shown in Figure 6a. Figures 8 and 10 show the vertical crustal structures, which delineate the sedimentary basin structures, for profiles N-N′ and S-S′, respectively. Figures 9 and 11 show vertical velocity structures extending down to mantle depths of 120 km, for profiles N-N′ and S-S′, respectively. Figure 12 is a four-panel spread showing the vertical velocity structure along all four of the linear segments shown in Figure 6a. Figures 8-12 also include the Bouguer gravity anomalies (Aldouri and Keller, 2011). In Figures 8-12, the red line indicates the Moho depth obtained from the joint receiver function/surface wave inversion model and the gray shaded areas at the top show the surface gravity anomaly (Aldouri and Keller, 2011).

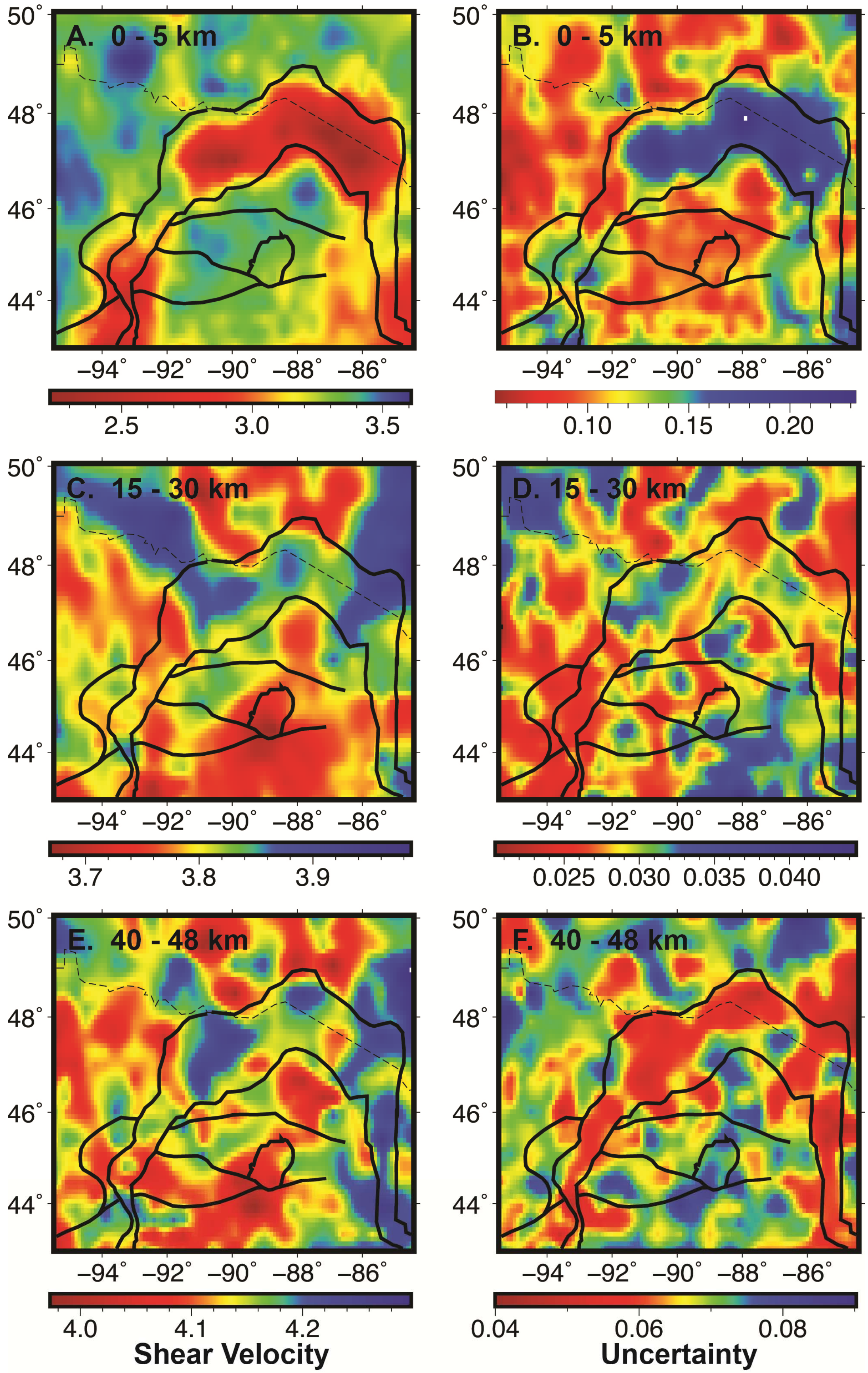

A. 0 - 5 km
B. 0 - 5 km
C. 15 - 30 km
D. 15 - 30 km
E. 40 - 48 km
F. 40 - 48 km
50°
48°
46°
44°
−94° −92° −90° −88° −86°
2.5 3.0 3.5
0.10 0.15 0.20
3.7 3.8 3.9
0.025 0.030 0.035 0.040
4.0 4.1 4.2
0.04 0.06 0.08
Shear Velocity
Uncertainty

468

Figure 6. Maps of the estimated shear velocity models and their uncertainties at three depths within the crust and three depths within the mantle: (a, b) averaged over 0-5 km; (c, d) averaged over mid-crustal depths (15-30 km); (e, f) averaged over lower crustal depths (40-48 km); (g, h) 70 km; (i, j) 90 km; and (l, m) 120 km. Panel 6a also shows the locations (N-N´ and S-S´) of the two linear SPREE arrays perpendicular to the MCR, the “SN” and “SS” profiles, whose vertical velocity profiles are shown in Figures 8-11, as well as the locations of the four quasi-along-axis profiles (BEG-M1-M2-M3-END) shown in Figure 12.

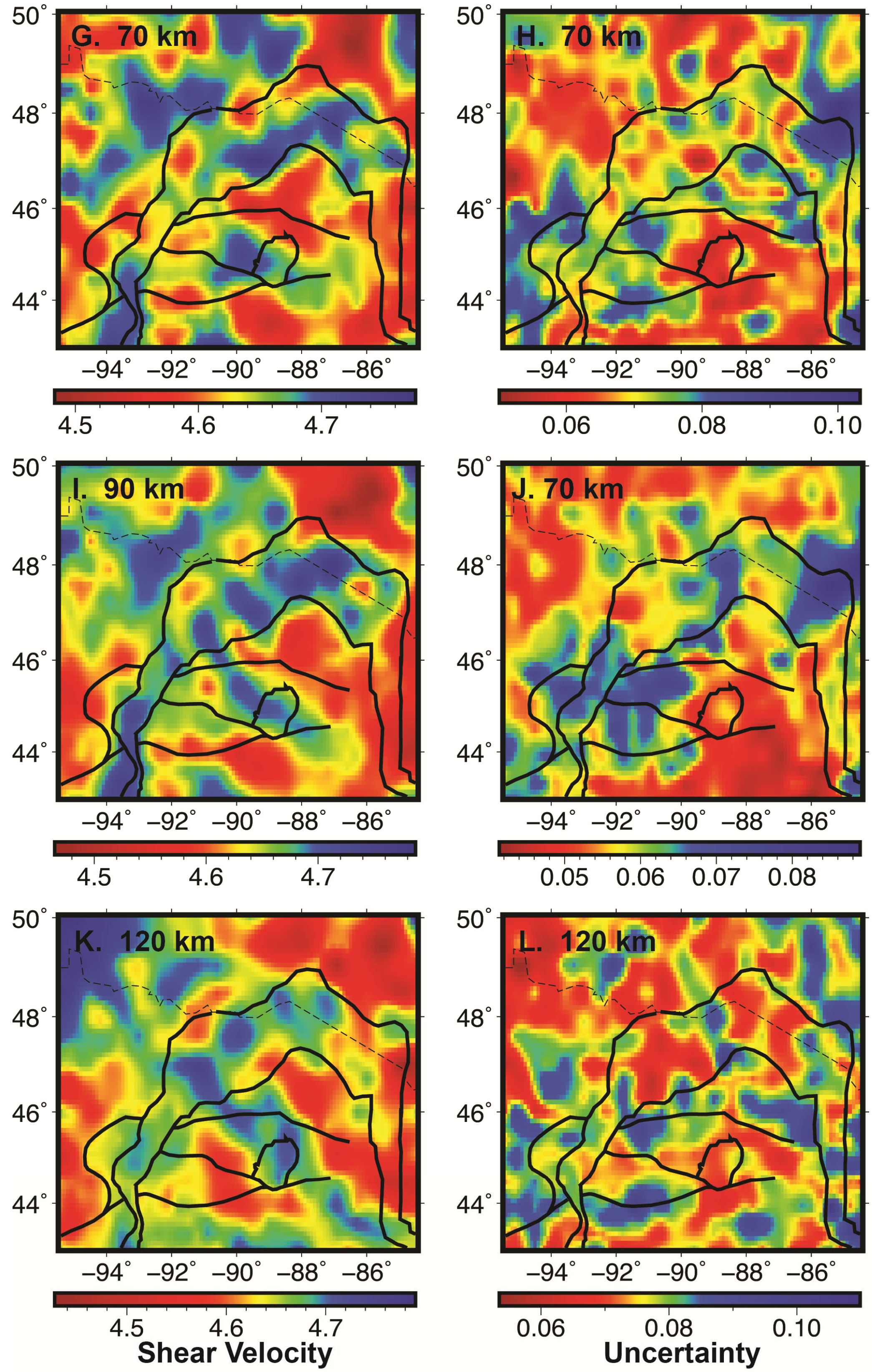

Figure 6. (Cont.)

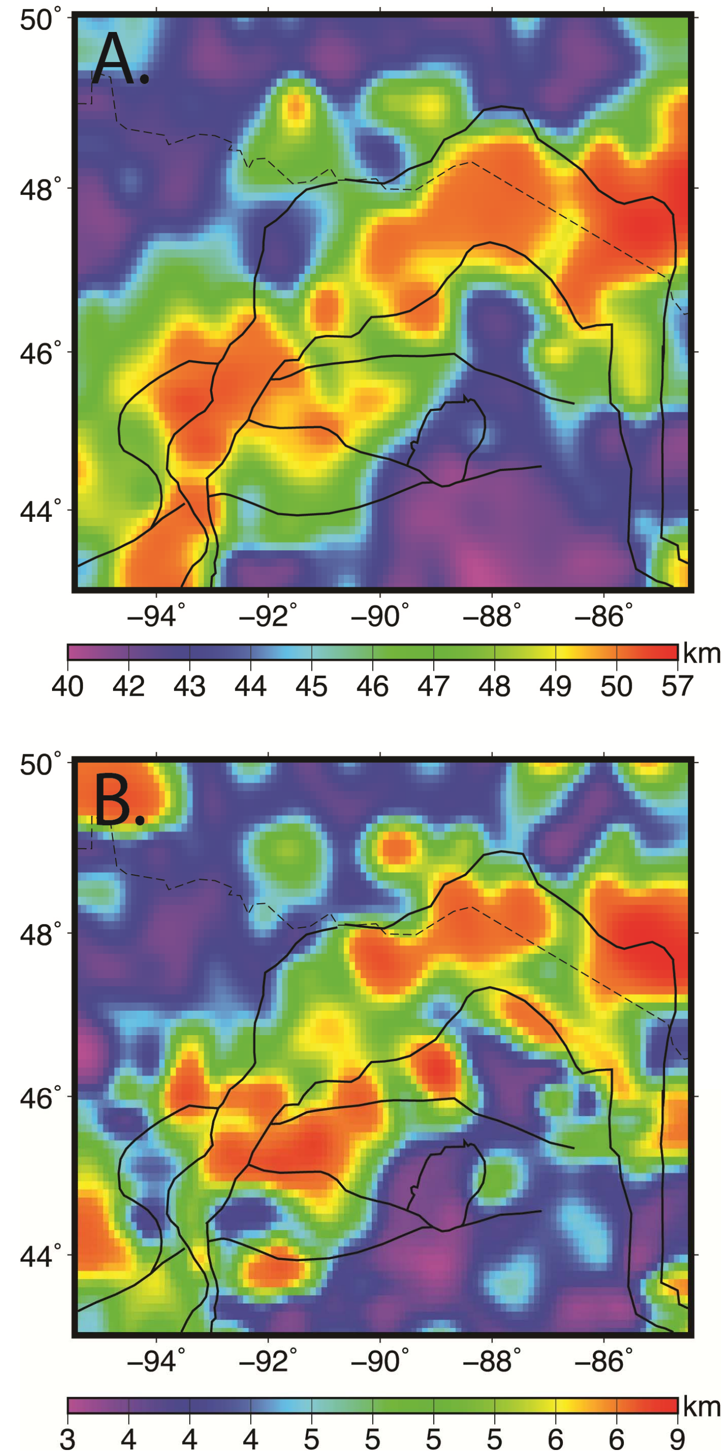

Figure 7. (a) Map of crustal thickness (depth to Moho, in km) resulting from the joint inversion of receiver functions and Rayleigh wave dispersion curves across the grid of nodes. (b) Map of uncertainties, in km, of the crustal thickness. Crustal thicknesses are generally greatest along the MCR, typically reaching about 50 km. The highest values (upper right, NE of the MCR) also correspond to a region of the highest uncertainties and are not reliable.

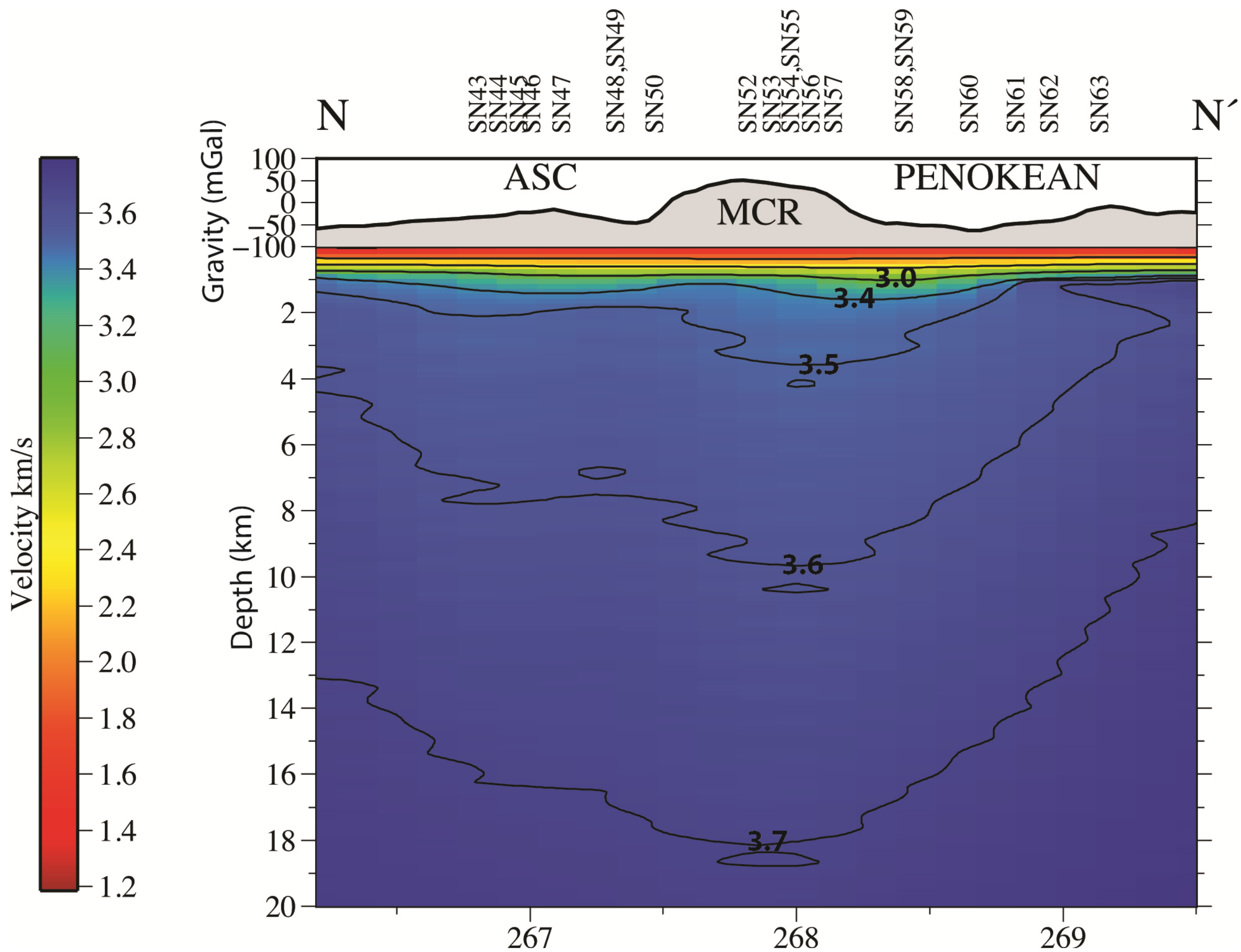

Figure 8. Vertical shear-wave velocity profile to a depth of 20 km through the 3-D model along the northern SPREE N-N´ transect shown in Figure 6a. The horizontal axis labels show the longitudes across the profile; the total length is about 330 km. The top (grey) curve shows the Bouguer gravity anomalies along the transect, in mgal (Aldouri and Keller, 2011). The location of the MCR is delineated at the top, as well as the locations of the Archean Superior Craton (ASC) and the Penokean orogenic rocks. Locations of the SPREE seismic stations are shown along the top. The shallow low-velocity layer at the top of the profile is interpreted as the remnant of the sedimentary and volcaniclastic rocks filling the MCR.

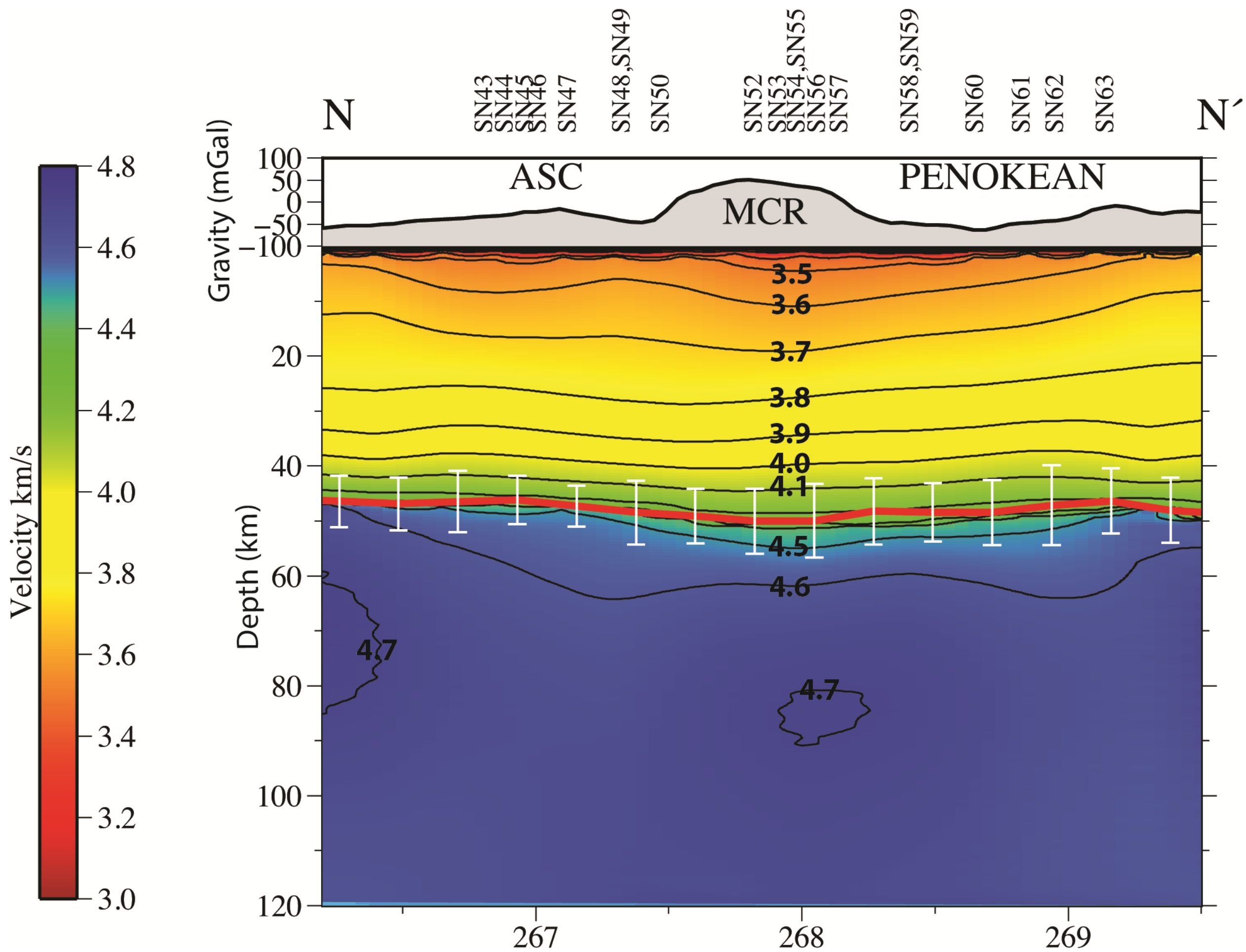

Figure 9. Similar to Figure 8, but extending to a depth of 120 km. The yellow line is the smoothed Moho depth, with the uncertainties from the inversion shown as vertical white lines. The top (grey) curve shows the Bouguer gravity anomalies along the transect, in mgal (Aldouri and Keller, 2011). The layer at the base of the crust with velocities between 4.1 and 4.6 km/s, interpreted as an underplated layer, is thickest beneath the MCR and narrows away from the rift.

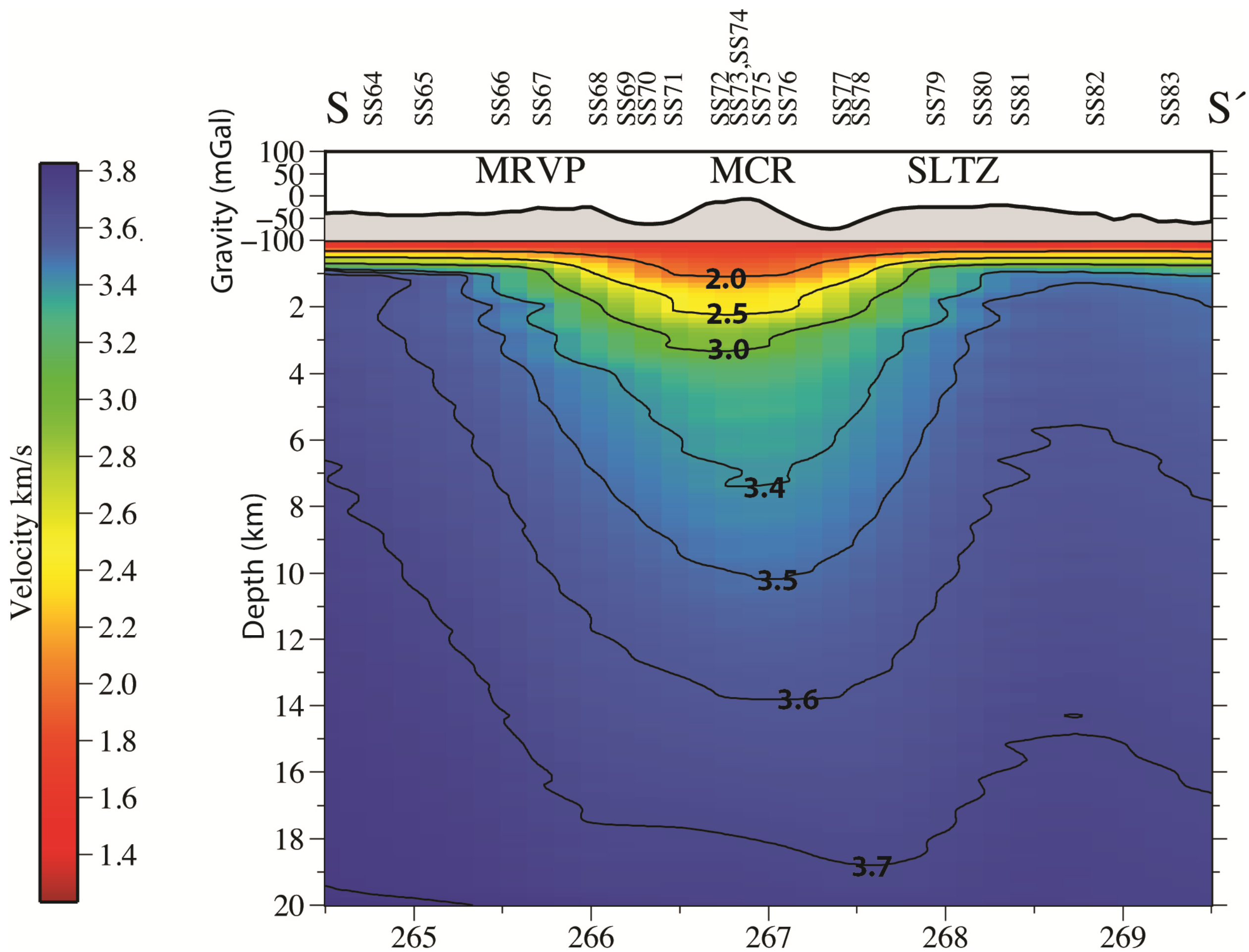

Figure 10. Vertical shear-wave velocity profile to a depth of 20 km, similar to Figure 8, but along the southern SPREE S-S´ transect. The total horizontal length covered is 400 km. The top (grey) curve shows the Bouguer gravity anomalies along the transect, in mgal (Aldouri and Keller, 2011). Also shown are the locations of the MCR and two adjacent tectonic features, the Archean Minnesota River Valley Province (MRVP) and the Spirit Lake Tectonic Zone (SLTZ).

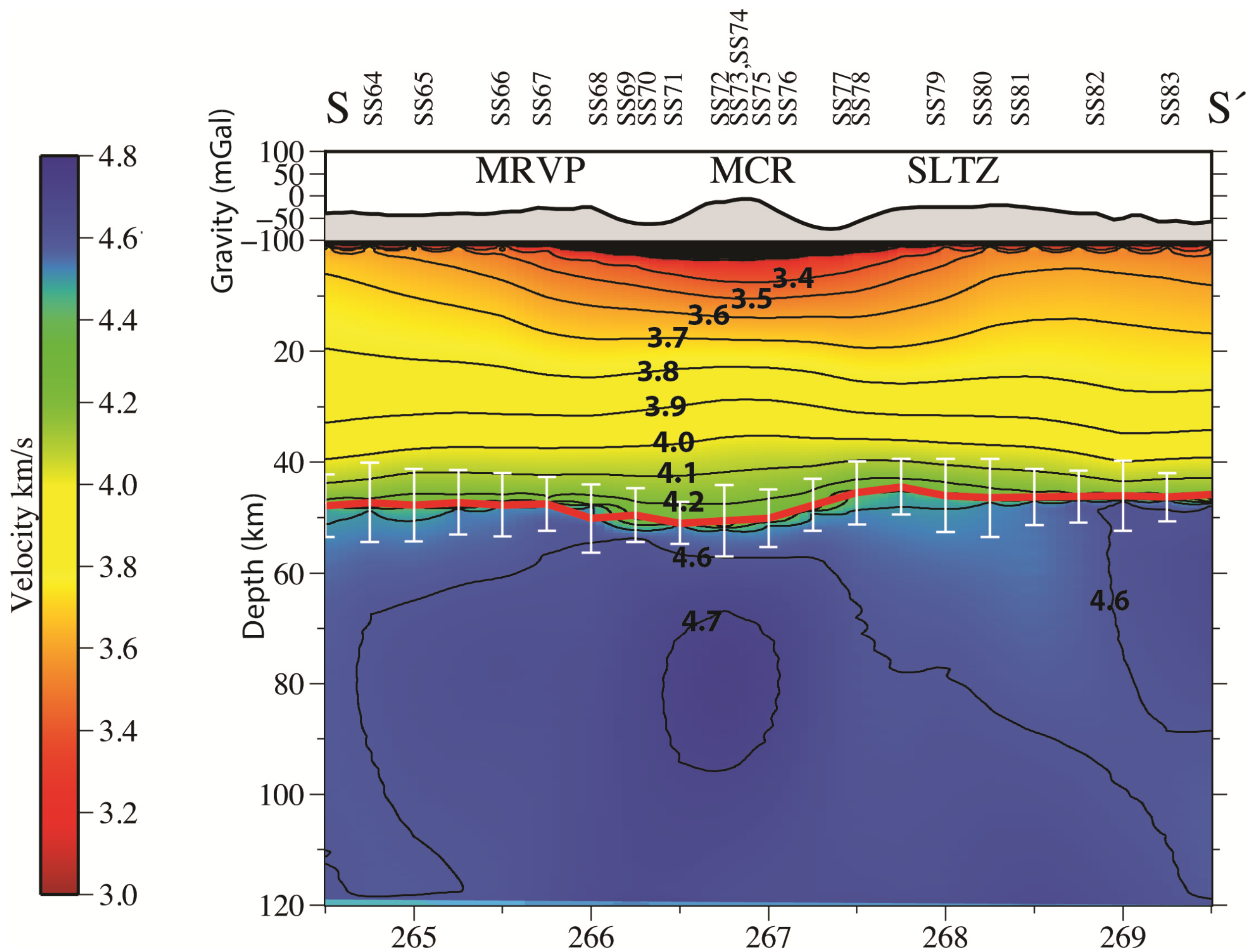

Figure 11. Similar to Figure 10, but now extending to 120 km in depth.

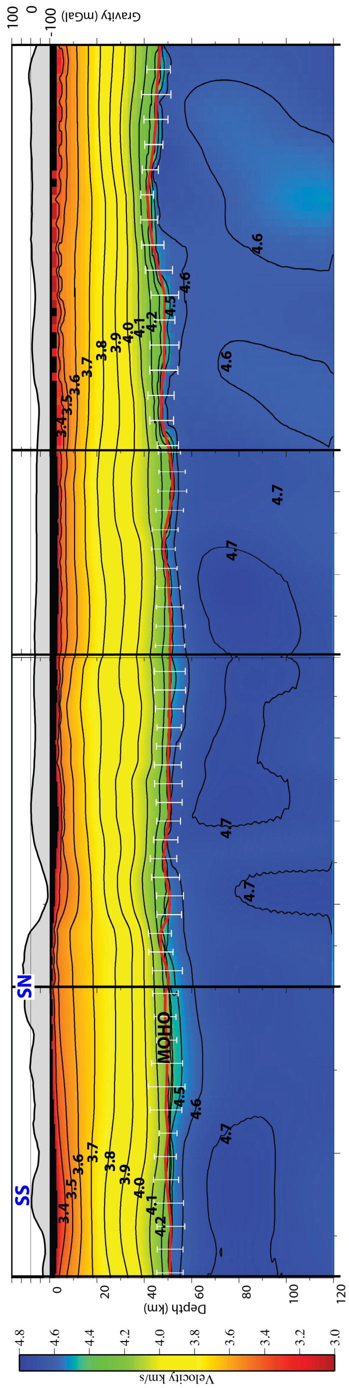

Figure 12. Similar to Figures 9 and 11, but along four transects that approximately parallel the rift (Figure 6a). Distances along the four linear profiles are 197 km, 231 km, 136 km, and 277 km, for a total length of 841 km. The locations where the southern ("SS") and northern ("SN") SPREE transects cross the profiles are labeled at the top.

4.1 Moho Depth

A smoothed map of Moho depths in Figure 7a shows variations in the crustal thickness of the MCR and surrounding regions, with uncertainties shown in Figure 7b. The inversion constrains the seismic velocities to vary continuously with depth. There is one exception to this, and that is in the case of the Moho. For one depth within the inversion, the seismic velocities are allowed to change discontinuously by any amount. The depth of the Moho discontinuity is one of the free parameters of the inversion, and so it can vary from location to location in order to best satisfy the combined RF and surface wave data. The uncertainties at each location are one standard deviation of the range in Moho depths for the 442 separate models retrieved from the Monte Carlo forward modeling. We found crustal thicknesses for the study region that ranged between 40 and 55 km, with the thickest along the MCR axis. This result agrees with the results of Shen et al (2013c) and Zhang et al. (2016) and with models of the history and evolution of the MCR characterized by early volcanism and subsequent massive sedimentation that built a thick crust beneath the rift valley.

Generally, the map shows two connected areas of significantly thicker crust along the MCR. These anomalies, trending roughly SW - NE, separate two regions of relatively average crustal thickness. The average-thickness regions, part of the Archean craton and bounding Paleoproterozoic orogenic belts, are located southeast and northwest of the rift and have a crustal thickness of about 40 km. The anomalously thick crustal regions are within the rift valley. In the Michigan Basin (the southeast part of the sampled region) crustal thicknesses were 39 – 43 km, with uncertainties of ±3 to ±6 km. North and northwest of the MCR, the crustal thickness has greater spatial variations ranging between 39 and 50 km, with uncertainties between ±5 and ±6.5 km.

Crustal thicknesses along the MCR are significantly greater than for surrounding regions, ranging in value from 50 – 55 km. Moho topography along the MCR varies spatially, with uncertainties between ±7 and ±10 km (Figure 7b). Variability in the MCR crustal thickness likely reflects the complexity of the rift evolution stages (Stein et al., 2015). Zhang et al. (2016) showed that both the bottom and top of the underplated layer can generate P-to-s conversions with variable observability, depending on the boundaries' topography and the back-azimuths of the teleseismic waves. It is possible that both boundaries were alternatingly selected by the

MCMC algorithm as representing the Moho. The high uncertainties in Moho depths beneath the MCR are consistent with structural uncertainties about the crust-mantle transition. The deepest Moho in our inversion, at a value of 55 km, is identified in the northeast of the sampled region. Another region of anomalously thick crust away from the MCR is at the southeastern corner of the sampled region. These values are not as well constrained, as they are at the edge of the study area and we have no receiver function data available for them.

Our inversion assumes a single “Moho” discontinuity. As discussed later, this may not be entirely appropriate where a thick layer of underplated intrusive volcanic material may have compositions and seismic velocities intermediate between the pre-rift crust and the mantle.

4.2 Shear Wave Velocity Structure from Joint Inversion

4.2.1 Velocities by Depth

In general, the images of the shear-velocity variations and their associated uncertainties in map views (Figure 6) and cross sections (Figures 8-12) show significant velocity variations that correlate with the location of the MCR.

In the shallow crust, between the surface and 5 km depth (Figure 6a), low velocities are associated with the sediments that overlie the volcanic rocks of the MCR. These velocities are variable along the rift axis, being observably slower in the northern part of the study (along M1-M2-M3) and in the south where profile S-S’ crosses the MCR. However, this is less evident where profile N-N’ crosses the MCR, which is consistent with along-rift variability in sedimentary layer thicknesses (Zhang et al., 2016).

Throughout the crust (Figures 6c and 6e) there are significant velocity variations. There is a tendency for faster velocities to be found within the along-axis profile, but it is very weak and not at all present along the N-N’ profile. Within the upper mantle, however, for all three maps (Figures 6g, 6i, and 6k) the MCR shows generally faster velocities for the BEG-M1-M2 segments (though not the eastern M2-M3 segment). The upper mantle velocities along the MCR are typically about 4.7 km/s, noticeably higher than background velocities, which are typically around 4.6 km/s. It is important to note that the MCR is not the only source of anomalous structure. At deeper mantle depths (70, 90, and 120 km) there appears to be a NW-SE-trending arm of anomalously fast velocities that cuts down across the Pembine-Wausau terrane, roughly perpendicular to the MCR.

4.2.2 Velocities Across the Rift Axis

The velocity structures of the sedimentary basins for the northern (Figure 8) and southern (Figure 10) transects are significantly different, in agreement with Zhang et al. (2016). In the northern transect (Figure 8), the sedimentary basin is only a little more than 1 km thick beneath the rift axis (in Zhang et al. [2016], the discontinuity for the bottom of the sub-rift sediment layer is at a depth of 1.5 km), and the thickest sediments occur at the edges of the central rift region. Evidence of a horst structure here due to post-rifting compression has been previously documented (Cannon et al., 1991; Cannon, 1994), and much of the central basin sediments have been uplifted along reverse faults and subsequently eroded. Along the southern transect, however (Figure 10), there appears to have been less uplift of the horst structure and the deepest sediments (>3 km) are found along the rift axis. This agrees with Zhang et al. (2016), who found the sub-rift discontinuity at the bottom of the sedimentary layer to be 3 km deep. Surface sedimentary basins in the region of study, such as the Michigan Basin at the southeast corner of the study area, show low seismic shear velocities.

Beneath the sedimentary layer, the two rift transects show slightly different patterns. In the northern transect (Figure 9), crustal velocities beneath the rift are mostly slightly lower than the surrounding regions, with isovels sloping upward in the direction away from the rift both eastward and westward. Shear velocities have largely leveled off by a depth of about 40 km, corresponding to the 4.0 km/s isovel. However, below the inversion-determined Moho discontinuity there again are slow velocities beneath the rift, with a thick layer of intermediate-to-fast shear velocities (up to 4.6 km/s) extending to about 65 km at its deepest (across much of the extended rift region). This layer of intermediate velocities, faster than the other lower crustal velocities but slower than the average upper mantle velocities for this region, pinches out entirely at the west end of the profile and nearly entirely at the east end of the profile. Directly beneath the rift axis, at a depth of about 80-95 km, a velocity reversal is found with velocities slightly faster (>4.7 km/s) than those above or below. Nowhere within the crust beneath the rift axis are fast velocities identified.

The situation is similar but slightly different along the southern east-west transect across the MCR (Figure 11). There is a more pronounced low-velocity sedimentary basin beneath the MCR axis. The isovels continue to dip toward the rift axis down to a depth of about 18 km, but then the trend reverses. From a depth of 18 km to about 40 km velocities are faster directly beneath the rift than for the surrounding two sides; the isovels slope upward toward the rift axis. Along the west side of the profile, velocities increase away from the rift axis at depths of 18 - 30 km (the isovels slope upward toward the west). However, this feature ends at a depth of 30 km, and from 30-40 km the fastest velocities are beneath the center of the rift. As with the northern profile, this region is underlain by slower velocities, from 40 km to almost 55 km in depth. These slower velocities beneath the rift axis (compared to the east and west extensions) occurs for a slightly different range of velocities: 4.1 – 4.5 km/s. As with the northern transect, this sub-rift layer of intermediate velocities is underlain by a region of fast (>4.7 km/s) velocities. The fast velocities start at a shallower depth (~55 km), peak at about 80 km, and extend over a greater depth range, with sub-rift velocities still faster than regions to the east and west to at least 120 km in depth.

4.2.3 Velocities Along the Rift Axis

Figure 12 depicts a vertical profile along the rift of shear velocities in the crust and upper mantle, similar to the cross-rift profiles in Figures 8 and 10. Figure 6a shows the locations of the four panels. The inversion generally aligns the Moho with the 4.4 km/s isovel, although the Moho aligns with shear velocities as low as 4.2 km/s (just south of the M1 marker, which represents the intersection with the northern east-west transect shown in Figure 10) and as high as 4.6 km/s (in the middle of the M1-M2 segment). This is appropriate in light of previous studies (Shen and Ritzwoller, 2016; Chichester et al., 2018) that found the normal Vs of the uppermost mantle in the MCR region to be between 4.4 and 4.5 km/s. The inversion-generated Moho depth along the rift axis is around 50 km for most of the profile (the three western segments), but shallows in the eastern segment (M3-END) to a minimum of 40 km.

Velocities are relatively constant along the MCR axis for the western three segments (BEG-M1-M2-M3), but Figure 12 shows some variations. The 4.0 km/s isovel is generally at a depth of about 40 km. However, between the M1 and M2 markers (northeast of the intersection of the N-N′ transect with the MCR) there is a region of anomalously low gravity that corresponds to lower upper-crustal velocities, increased lower-crustal velocities, and increased upper mantle velocities. There is significant variability in the depth of the 4.6 km/s isovel, the thickness between the 4.2 and 4.6 km/s isovels, and the distance between the Moho and 4.6 km/s isovel. As discussed next, this may indicate variations in the thickness of a layer of underplated intrusive igneous material.

The eastern arm of the MCR, represented by the M3-END panel, is significantly different from the rest of the MCR axis and more resembles non-MCR regional velocities. Gravity anomalies are close to zero, the Moho depth is close to a typical continental value of 40 km, and the upper mantle velocities are close to a typical stable-continental upper mantle value of 4.6 km/s. The latter is in contrast with the upper mantle velocities in the western three panels, which are closer to a speed of 4.7 km/s.

5 Discussion

5.1 Prevailing Models of the MCR

For more than thirty years, the predominant model for the MCR has been a thickened crust containing a few kilometers of surface sediments, a thick upper crust containing a mix of original continental materials and rift-fill mafic volcanics, and, beneath Lake Superior, an underplated lower crust extending to depths of 50-60 km (Hutchinson et al., 1990). These structures appear to be the result of continental rifting (the 1.1 Ga Keweenawan rifting event) coincident with a large volume of syntectonic volcanic activity, followed by compressional faulting causing the uplift of a central horst along reverse faults and subsequent erosion of the exposed basin sediments.

One of the first seismic lines across the MCR was the 1986 deep crustal marine multichannel seismic reflection survey collected as part of the Great Lakes International Multidisciplinary Program on Crustal Evolution (GLIMPCE). Seismic analyses identified 2 km of sediments sitting atop a >30-km-thick segment of volcanics (Vp 5.2-7.2 km/s) underlain by up to 20 km of underplated lower crust (Vp 7.0-7.3 km/s) down to a maximum sub-axis depth of 55 km (Shay and Trehu, 1993; Hamilton and Mereu, 1993). Combining the seismic analyses with gravity data (Klasner et al., 1979; Thomas and Teskey, 1994) and petrological analyses of exposed Keweenawan volcanics (Halls, 1969; Lippus, 1988), as well as the incorporation of geophysical interpretations of other MCR seismic lines (Chandler et al., 1989) provided the basis for models involving a large volume (up to 1.3 million km^3) of hot spot-derived volcanic rift in-fill as well as a dense (3.08 g/cm^3) layer of underplated lowermost crust (Hutchinson et al., 1990).

To a very large degree, our inversion results support this model. Most previous studies were done with high-frequency local P waves, which have strong resolution for multiple reflectors but limited depth penetration. Modeling surface waves for the shear velocity structure, even in the same location, would be expected to resolve different features both because of the difference in frequencies and the different response to longitudinal and shear waves. For example, mafic rift volcanics tend to have high Vp/Vs ratios (Thybo and Artemieva, 2013), so crustal volcanics that appear as fast anomalies with P waves may not be observable with S waves (Schulte-Pelkum et al., 2017). Surface wave studies using EarthScope TA data have not generally found evidence of faster crustal shear velocities within the MCR footprint. Shen and Ritzwoller (2016) found no significant evidence of fast crustal shear velocities and Schmandt et al. (2015) actually found generally lowered crustal shear velocities, which could result from the presence of high-density volcanic layers with otherwise typical shear moduli, or could possibly also be a result of anisotropic anomalies within the crust. Our results support slightly elevated crustal velocities beneath the rift, with no evidence of slow velocities. The lack of mid- and upper-crustal seismic anomalies may be expected based upon the magmatic differentiation process, whereby intruded volcanics may become increasingly felsic as they rise through the crust and generate differential crustal melting (Miller and Nicholson, 2013). Past observations of velocities along the MCR axis vary significantly, which may be expected based on an episodic history of along-rift volcanic events including intruded batholiths and surrounding sill structures (Thybo and Artemieva, 2013). Our results agree with this.

5.2 Observations of and Explanations for Crustal Underplating

One of the most noticeable variations we observe is in the thickness of the layer that spans seismic velocities from 4.1 to 4.6 km/s, which may be associated with a layer of underplating (Thybo and Artemieva, 2013). This is especially visible in Figure 12, where the distance between the 4.1 and 4.6 km/s isovels varies in thickness from less than 10 km to more than 20 km. Figure 12 also shows that although the Moho depth, which is a free parameter separate from the velocities within the inversion (where the velocity is allowed to increase discontinuously), generally aligns with the 4.4-4.5 km isovels, its location varies between 4.2 and 4.6 km/s in order to best model the RF and surface wave data. In areas without the history of a magmatic event there is generally a large jump in seismic velocities across a relatively narrow Moho depth range, from lower crust values of Vp < 7.0 km/s and Vs < 4.0 km/s (Holbrook et al., 1992; Rudnick and Fountain, 1995) to typical upper mantle velocities of Vp ≅8.0 km/s and Vs ≅4.6 km/s. However, this is not the case for areas that have undergone magmatic underplating, consistent with our results.

Various tectonic and igneous processes may lead to underplating within the continental lithosphere (White and McKenzie, 1989; Thybo and Artemieva, 2013), which can theoretically take the form of magma ponding at the base of the continental crust but more commonly consists of the emplacement of igneous sills and batholiths within the lowermost crust and/or uppermost mantle (Thybo and Artemieva, 2013). The emplaced lower crustal mafic rocks have anomalously high densities, in part because of the fractionation of lighter materials that leave the lower crust and migrate to the upper crust. The depleted lower crustal intruded mafic material is typically identified by higher densities, higher P- and S-wave velocities, and a high Vp/Vs ratio, when compared to ultramafic rocks (Christensen, 1996). However, fewer Vs measurements of underplated regions are available compared to Vp data, so the available Vp/Vs data set is very limited.

However, an interpretation based on these characteristics is not unique because of the possible presence of lower crustal granulite rocks that that have been metamorphosed into phases such as eclogite or serpentinized peridotite (Thybo and Artemieva, 2013). There is inherent uncertainty as to the process of emplacing an underplated layer in a continental rift. A common hypothesis is that magma intrudes into the lower crust, increasing the crustal velocities. The mass of the extrusive volcanics that fill the rift depresses the crust, lowering the Moho. The underplating could also occur through infiltration of the upper mantle, decreasing uppermost mantle velocities. In this case, what is considered to be lower crust now extends into the top part of the former uppermost mantle and the new Moho is the boundary between the undisturbed and volcanically infiltrated mantle. As a result of underplating, the seismic Moho may no longer represent a compositional boundary at the base of a primitive continental crust but rather a seismic and density boundary between rocks of differing metamorphic states (Mengel and Kern, 1992).

The seismic velocities of underplated layers can be variable but are typically in the 7-8 km/s range for P velocities and 4-4.6 km/s range for S velocities, leading them to be called the 7.X or 4.X layers (Schulte-Pelkum et al., 2017). It is instructional to compare the depth and thickness of the MCR underplated layer to those layers found in other parts of the world, in both rifted and non-rifted tectonic settings. Underplated layers are usual for both areas of hot spot volcanism (Olugboji and Park, 2016) and continental rifting, with the thickness of the layer generally much greater for less-stretched rifting than more-stretched areas (Collier et al., 1994). Underplated layers at the base of the crust (or top of the upper mantle) have been identified beneath the Hartford Basin (up to Vs 4.5 km/s, up to 15 km in thickness; Gao et al., 2020) Baltic Shield (Vp 7.2-7.5 km/s, depth from 35 to 55 km; Korsman et al., 1999), Hatton Bank in the NE Atlantic (Vp 7.3 km/s; Fowler et al., 1989), Ukrainian Shield (Vp 7.6 km/s, 10 km thick; Thybo et al., 2003), Oslo Graben (Vp 7.3-7.4 km/s; Thybo and Artemieva, 2013), Medicine Hat block (Vp 7.5-7.9 km/s; Clowes et al., 2002), North China Craton (Vs 3.8-4.2 km/s, Vp/Vs > 1.78; Tian and He, 2021), and Laccadive Island (from the Reunion Hotspot) (Vs 4.25-4.4 km/s and 8 km thick, where the uppermost mantle is 4.6 km/s; Gupta et al., 2010). However, it is also important to note that evidence of underplating is not always seen in analyses of Moho velocity structure for rifted regions, such as for the continental rifting beneath the South Georgia basin (Marzen et al., 2019).

5.3 Crustal Underplating Beneath the MCR

For the MCR, the combination of seismic and gravity anomalies of Lake Superior has been interpreted as underplating in the lower crust up to 15 km thick (Behrendt et al., 1990; Hinze et al., 1992; Shay and Trehu, 1993; Hamilton and Mereu, 1993; Hutchinson et al., 1990, 1992; Zhang et al., 2016). Behrendt et al. (1990) and Hutchinson et al. (1992) proposed that the high-velocity material that makes up the present-day lower crust was probably originally mantle material that now appears to have crustal properties because of the large volume of intruded gabbroic rocks. Although there are often multiple seismic reflectors within the underplated layer, its upper and lower boundaries usually display distinct seismic reflectors that are seen as both normal-incidence and wide-angle reflections (Thybo and Artemieva, 2013).

The shear velocities from our surface wave inversion provide a new form of support for the idea of sub-crustal underplating, given the higher spatial resolution provided by the co-deployment of SPREE and TA stations. Previous shear velocity studies of the Midwest U.S. did not identify such a layer. Neither the iterative surface wave and multimode receiver function shear velocity model of Schmandt et al. (2015) nor the joint surface wave / receiver function inversion model of Shen and Ritzwoller (2016) show evidence of fast lowermost crustal velocities. For both of these long-wavelength models, the lowermost crust has Vs < 4.2 km/s, and in both models the MCR does not show anomalous lower crustal shear velocities.

Neither Schmandt et al. (2015) nor Shen and Ritzwoller (2016) found anomalous upper mantle velocities beneath the MCR. In Shen and Ritzwoller (2016), average uppermost mantle velocities (taken as the average over the top 8 km of the mantle beneath the Moho) under eastern Iowa and the central Dakotas reach as high as 4.6 km/s, but in the footprint of the MCR across Minnesota, Wisconsin, and Iowa, the averaged uppermost mantle velocities are between 4.4 – 4.5 km/s. We use the same inversion process and also observe that the uppermost mantle velocities (in relation to the inverted Moho depth) are generally 4.4 – 4.5 km/s. However, this may be an artifact of the inversion allowing only one large discontinuous increase in the region of the Moho. It is possible that there are essentially two Moho-like boundaries, at the top and bottom of the underplated layer.

5.4 Moho Structure Across the Northern Transect

Two recent studies focusing on the SPREE receiver functions found evidence for a double-Moho: Zhang et al. (2016) (which we will refer to Z16) and Chichester et al. (2018) (here referred to as C18). Both found multiple discontinuities at depths that varied along the SPREE profiles. Along the northern cross-rift profile (SN), Z16's analysis of P-to-S (Ps) conversions found a strong single Moho discontinuity away from the MCR at a depth of about 40 km. However, as this interface approached the MCR it deepened, weakened in resolution, and split into two, with one set of positive (increasing velocity) discontinuities continuing to a depth of about 55 km and another set of positive discontinuities emerging at a depth of around 37 km. They interpreted this 18-km thick zone between the two discontinuities as the underplated zone of intruded volcanics.

Also along the northern SPREE transect, C18, who used S-to-P (Sp) conversions, found no substantial evidence of topography on the Moho as it crossed the rift, varying only slightly between 34 and 38 km in depth. However, they observed a weakening of the conversion beneath the rift compared to the two flanks. The complete Sp data set did not show a deeper positive discontinuity, but when only phases from earthquakes in the 55-60° distance range were used, a second positive discontinuity was observed at a depth of 61 km, analogous to the 55-km Ps discontinuity observed by Z16.

Given the nature of our inversion, our results are in general agreement with both of these studies. We allow for only one Moho discontinuity, and in the northern transect, our inversion locates this positive discontinuity at a depth of 50 km, halfway between the two positive discontinuities found by Z16 and C18 at about 40 km and 60 km depth. Shen et al. (2013c), which used a similar inversion to ours but without the SPREE data, also found a Moho depth of 50 km where our northern transect crosses the MCR.

Adding surface waves to receiver functions provides the ability to invert for the actual vertical velocity structures as well as discontinuity locations. We find evidence for the underplated layer not in the location of the Moho but rather in the change in the vertical spread of shear velocities across the profiles. Shear velocities generally vary by a small amount across most of the vertical extent of the crust, increasing by only 0.5 km/s (from 3.5 – 4.0 km/s) over a vertical range of 35 km (from 5 – 40 km depth). Away from the rift, there is a sudden increase across the Moho to the 4.6 km/s velocities at the top of the mantle. However, this jump vertically broadens beneath the rift. For example, at the left side of Figure 9 the 4.2 and 4.6 km/s isovels nearly merge, but the distance between them increases to ~15 km beneath the MCR. If the 4.0 km/s and 4.6 km/s isovels represent the top and bottom of an underplated zone (Holbrook et al., 1992; Schulte-Pelkum et al., 2017), then our velocities suggest an underplate about 20 km thick (4.0 km/s at a depth of 40 km and 4.6 km/s at a depth of 60 km). Profile A-A’ of Shen et al. (2013c) is not at the exact same location as the northern SPREE transect (slightly to the south and with a more W-E trend), but also shows shear velocity evidence of an underplated layer about 20 km thick (40 km – 60 km in depth) under the MCR.

5.5 Moho Structure Across the Southern Transect

The southern W-E SPREE transect crosses the MCR in a location with different characteristics than the northern transect. The northern transect crosses the MCR at a location with a relative gravity high (+50 mgal, Figure 9). However, the gravity anomaly where the southern SPREE transect crosses the MCR, although still slightly higher than the adjacent areas, is only at 0 mgal (Figure 11), largely reflecting the thicker surface sedimentary layer. The overall velocity structure along the southern transect is also generally different than the northern transect: velocities in the mid-crust are faster, and velocities at the top of the mantle are slower. Accordingly, the 4.5 km/s isovel may be a better indicator of the bottom of an underplate. Figure 11 shows that the vertical distance between the 4.0 and 4.5 km/s isovels increases from about 10 km at the west and east ends of the profile to about 20 km beneath the MCR, extending to a depth of ~55 km, suggesting a thinner underplated layer than along the northern transect and one that is slightly elevated.

This is still in general agreement with Z16 and C18. For the southern SPREE transect, Z16 finds a slightly more complex set of lower crustal discontinuities, but in general there is again a strong positive Ps discontinuity at a depth of 43 +/- 7 km away from the rift that shallows to ~35 km beneath the rift, with an additional positive Ps discontinuity that drops to ~60 km depth at the center of the MCR. C18 finds an Sp discontinuity beneath the rift at 35-37 km depth, in agreement with Z16 and our shallower 4.0 km/s isovel. However, unlike for Z16, C18 does not see a deeper ~60-km-deep discontinuity using Sp data, perhaps reflecting the more complex deep structures that we also identify beneath the southern transect.

5.6 Moho Structure Along the Rift Axis

Along the rift axis, Figure 7 of Z16 shows the receiver function discontinuities for stations SM17-SM42 and evidence for a double-discontinuity underplated layer along the full length. The discontinuities shallow toward the north but the distance between them stays about 10-20 km in thickness. The Z16 discontinuities are deepest for the rift stations near where the southern transect crosses the rift (between stations SM39 and SM40), between about 45 and 65 km depth. The thickness of the proposed underplated layer is still about 20 km in the region surrounding where the northern transect crosses the rift (between stations SM21 and SM22), but the range is now from ~33 to 50 km in depth. At the far north end of the rift, as covered by the

SPREE stations, approaching station SM17 the underplated layer is both narrowest and shallowest. Our results generally agree with these values.

The four linear profiles in our Figure 12 do not exactly align with the rift and are therefore not directly comparable to Figure 7 of Z16. These profiles cross the southern SPREE transect at the “SS” label and cross the northern SPREE transect at the “SN” label (also the M1 location). The variations in isovel location are partly a function of distance from the MCR, so direct determination of along-rift variations is not possible. Along the quasi-rift-parallel profiles there is a significant low-velocity layer of a few kilometers at the surface, representing the rift-fill sediments. These range from about 1.5 km in thickness (in the transect crossing at SN) to more than 3 km (in the transect crossing at SS), which may result from a combination of rifting history and post-rifting compressional uplift. There is a general tendency for the crustal and upper mantle isovels to shallow toward the north of the profiles (from BEG to M3), and then again going south down through the eastern arm of the MCR (from M3 to END).

5.7 Moho Structure Away From the Rift

Away from the rift, we observe a trend of crustal thinning toward the southeast and northwest, moving away from the rift. This supports the observations of Shen at al. (2013c) and proposals by multiple studies (e.g., Stein et al., 2011, 2016, 2018; Zhang et al., 2016) that the MCR represents a roughly >100-km-wide zone of crustal thickening by some combination of magmatic underplating in either (or both) of the lowermost crust or uppermost mantle during the magmatic phase and the depression of the crust by a combination of extrusive volcanic infill of the rift and reverse faulting during a later episode of compression and crustal shortening.

7 Conclusions

Analysis combining receiver function and surface wave dispersion data in the region of the U.S. Midcontinent Rift (MCR) resolves velocities that help provide a basis for the interpretation of the crustal and upper mantle structure along and near the MCR. In general, seismic velocities in the upper crust are slower beneath the MCR than away from it. Below the mid-crust (15-30 km depth) velocities in the mid-crust are generally faster beneath the MCR than in the areas surrounding it. The velocities in the lowermost crust are also generally faster beneath the MCR, opposite of what would be expected if the only structural anomaly deep beneath the

MCR was a deepening of the crust. We find a deepening of the Moho beneath the MCR to depths of at least 50 km, from a regional average of about 40 km. Hence we might expect crustal velocities along the rift to be lower than the upper mantle velocities at this depth away from the rift. However, we instead find a thick layer, from about 40-60 km in depth, of transitional velocities between 4.1 - 4.6 km/s, a velocity range expected for underplated mafic volcanic material with velocities intermediate between typical lower crust and upper mantle material. These results are consistent with, but provide much greater spatial coverage and velocity resolution, than earlier studies of the MCR and rifts elsewhere. Future study directions should including inverting the surface wave and receiver function data with explicit parameterizations for discontinuous velocity increases, in essence a double-Moho, at both the top and bottom of this underplated layer. We also find anomalously high shear-wave velocities 70-90 km below the rift, suggesting the presence of depleted upper mantle material.

Acknowledgments

This study is supported by the NSF grants EAR-1148088 and EAR-0952345. Our thanks are extended to many national parks and landlords in Canada and USA who allowed us to disturb their yards and temporarily deploy seismometers. Our thanks extend to Trevor Bollmann, Patrick Shore, Emily Wolin, and multiple field assistants for the installation, maintenance, service, and demobilization of the SPREE seismometers. The seismic instruments were provided by the Incorporated Research Institutions for Seismology (IRIS) Portable Array Seismic Studies of the Continental Lithosphere (PASSCAL) Instrument Center and EarthScope USArray Array Operations Facility (AOF). Some figures were made using the GMT software (Wessel et al., 2013). We thank Associate Editor Michael Bostock and two anonymous reviewers for their thorough, insightful, and patient reviews, the changes in response to which significantly improved the readability of this paper.

Open Research

The facilities of IRIS Data Services, and specifically the IRIS Data Management Center (DMC), were used for access to waveforms, related metadata, and/or derived products used in this study. Data from the TA network were made freely available as part of the EarthScope USArray facility, operated by Incorporated Research Institutions for Seismology (IRIS) and

supported by the National Science Foundation, under Cooperative Agreements EAR-1261681. These data can be accessed at DOI 10.7914/SN/TA. The data from the SPREE Flexible Array (http://www.usarray.org/researchers/obs/flexible/deployments/1116_SPREE/) can be obtained at http://www.usarray.org/researchers/data with the network code SPREE-XI.

References

Aldouri, R., & Keller R. (2011). Development of robust data system for gravity and magnetic anomaly data: A case study of a community-based effort for point data. *Geoinformatics*, Cambridge University Press.

Allen, D. J., Braile, L. W., Hinze, W. J., & Mariano, J. (1995). The Midcontinent rift system, U.S.A.: A major Proterozoic continental rift. In K. H. Olsen (Ed.), *Continental rifts: evolution, structure, tectonics* (pp. 372-407). New York, NY: Elsevier.

Allen, D. J., Hinze, W. J., Dickas, A. B., & Mudrey, J. M. (1997). Integrated geophysical modeling of the North American Midcontinent Rift System: New interpretations for western Lake Superior, northwestern Wisconsin, and eastern Minnesota. In R. W. Ojakangas, A. B. Dickas, & J. C. Green (Eds), *Middle Proterozoic to Cambrian rifting, central North America* (pp. 47-72). Boulder, CO: Geological Society of America.

Barmin, M. P., Ritzwoller, M. H., & Levshin, A. L. (2001). A Fast and Reliable Method for Surface Wave Tomography. *Pure and Applied Geophysics,* **158**(8), 1351-1375. https://doi.org/10.1007/pl00001225.

Behrendt, J. C., Green, A. G., Cannon, W. F., Hutchinson, D. R., Lee, M. W., Milkereit, B., Agenea, W. F., & Spencer, C. (1988). Crustal structure of the Midcontinent rift system: Results from GLIMPCE deep seismic reflection profiles. *Geology,* **16**(1), 81-85. doi: https://doi.org/10.1130/0091-7613(1988)016<0081:CSOTMR>2.3.CO;2

Behrendt, J. C., Hutchinson, D. R., Lee, M., Thornber, C. R., Tréhu, A., Cannon, W., & Green, A. (1990). GLIMPCE Seismic reflection evidence of deep-crustal and upper-mantle intrusions and magmatic underplating associated with the Midcontinent Rift system of North America. *Tectonophysics*, **173**(1–4), 595-615. https://doi.org/10.1016/0040-1951(90)90248-7.

Bensen, G. D., Ritzwoller, M. H., Barmin, M. P., Levshin A. L., Lin, F., Moschetti, M. P., Shapiro, N. M., & Yang, Y. (2007). Processing seismic ambient noise data to obtain reliable broad-band surface wave dispersion measurements. *Geophysical Journal International*, **169**(3), 1239–1260. https://doi.org/10.1111/j.1365-246X.2007.03374.x

Bollmann, T. A., van der Lee, S., Frederiksen, A. W., Wolin, A. E., Revenaugh, J., Wiens, D. A., Darbyshire, F. A., Stein, S., Wysession, M. E., & Jurdy, D. (2019). P-wave teleseismic traveltime tomography of the North American Midcontinent. *J. Geophys. Res*., **124**, 1725-1742, 10.1029/2018JB016627.

Boyd, N. K., & Smithson, S. B. (1993). Moho in the Archean Minnesota gneiss terrane: Fossil, alteration, or layered intrusion? *Geology,* **21**(12), 1131-1134.

Cambray, F. W. & Fujita, K. (1991). Collision Induced Ripoffs, Ancient and Modern: The Midcontinent Rift System and the Red Sea-Gulf of Aden compared. Abstract retrieved December 12, 2017, from http://www.d.umn.edu/Prc/lakesuperiorgeology/Volumes/ILSG_37_1991_pt1_Eau_Claire.CV.pdf

Campbell, I. H. (2001). Identification of ancient mantle plumes. In R. E. Ernst & K. L. Buchan (Eds), *Mantle plumes: their identification through time* (Vol. 352). GSA Special Papers. https://doi.org/10.1130/0-8137-2352-3.5

Cannon, W. F. (1994). Closing of the Midcontinent rift-A far—field effect of Grenvillian compression. *Geology,* **22**(2), 155.

Cannon, W. F., Green, A. G., Hutchinson, D. R., Lee, M., Milkereit, B., Behrendt, J. C., Halls, H. C., Green, J. C., Dickas, A. B., Morey, G. B., Sutcliffe, R. & Spencer, C. (1989). The North American Midcontinent rift beneath Lake Superior from GLIMPCE seismic reflection profiling. *Tectonics,* **8**(2), 305-332.

Cannon, W. F., Lee, M. W., Hinze, W. J., Schulz, K. J., & Green, A. G. (1991). Deep crustal structure of the Precambrian basement beneath northern Lake Michigan, midcontinent North America. *Geology,* **19**(3), 207-210.

Chandler, V.W., & Lively, R.S. (2011). Upgrade of the Gravity Database. Retrieved from the University of Minnesota Digital Conservancy. https://hdl.handle.net/11299/163539.

Chandler, V. W., McSwiggen, P. L., Morey, G. B., Hinze, W. J., & Anderson, R. R. (1989). Interpretation of Seismic Reflection, Gravity, and Magnetic Data Across Middle Proterozoic

Mid-Continent Rift System, Northwestern Wisconsin, Eastern Minnesota, and Central Iowa. *AAPG Bulletin,* **73**(9), 261-275. https://doi.org/10.1306/703c9b68-1707-11d7-8645000102c1865d

Chichester, B., Rychert, C., Harmon, N., van der Lee, S., Frederiksen, A., & Zhang, H. (2018). Seismic imaging of the North American Midcontinent Rift using S-to-P receiver functions. *Journal of Geophysical Research: Solid Earth*, **123**, 7791–7805. https://doi.org/10.1029/2018JB015771

Christensen, N.I. (1996). Poisson's ratio and crustal seismology. *Journal of Geophysical Research,* **101**, 3139–3156.

Clowes, R. M., Burianyk, M. J. A., Gorman, A. R., & Kanasewich, E. R. (2002). Crustal velocity structure from SAREX, the Southern Alberta Refraction Experiment. Canadian Journal of Earth Sciences, **39**(3), 351-373. Doi:10.1139/e01-070.

Davis, D. W., & Green, J. C. (1997). Geochronology of the North American Midcontinent rift in western Lake Superior and implications for its geodynamic evolution. *Canadian Journal of Earth Sciences,* **34**(4), 476-488. https://doi.org/10.1139/e17-039

Davis, W.R., Collins, M., Rooney, T., Brown, E., Stein, C., Stein, S., & Moucha, R. (2022). Geochemical, petrographic, and stratigraphic analyses of the Portage Lake volcanics: implications for the evolution of main stage volcanism in continental flood basalt provinces, *Geological Society, London, Special Paper*, **518**(1), 67-100, doi 10.1144/SP518-2020-221

Dickas, A. B. (1986). Comparative Precambrian Stratigraphy and Structure Along the Mid-Continent Rift. *AAPG Bulletin,* **70**(3), 225-238. https://doi.org/10.1306/9488566a-1704-11d7-8645000102c1865d

Dickas, A. B., & Mudrey, M. G., Jr**.** (1997). Segmented structure of the Middle Proterozoic Midcontinent Rift System, North America. In R. W. Ojakangas, A. B. Dickas, & J. C. Green (Eds), *Middle Proterozoic to Cambrian rifting, central North America* (pp. 37-46). Boulder, CO: Geological Society of America.

Elling, R., Stein, S., Stein, C., & Gefeke, K. (2022). Three major failed rifts in central North America: similarities and differences, *GSA Today*, https://doi.org/10.1130/GSATG518A.1

Foster, A., Darbyshire, F., and Schaeffer, A. (2020). Anisotropic structure of the central North American Craton surrounding the Mid-Continent Rift: Evidence from Rayleigh waves. *Precambrian Research*, **342**, 105662, https://doi.org/10.1016/j.precamres.2020.105662.

Fowler, S. R., White, R. S., Spence, G. D., & Westbrook, G.K. (1989). The Hatton Bank continental margin. 2. Deep-structure from 2-ship expanding spread seismic profiles. *Geophysical Journal of the Royal Astronomical Society,* **96**, 295–309.

French, S. W., Fischer, K. M., Syracuse, E. M., & Wysession, M. E. (2009). Crustal structure beneath the Florida-to-Edmonton broadband seismometer array. *Geophysical Research Letters*, **36**(8). https://doi.or10.1029/2008gl036331

Gao, H., Yang, X., Long, M. D., & Aragon, J. C. (2020). Seismic evidence for crustal modification beneath the Hartford rift basin in the northeastern United States. *Geophysical Research Letters*, **47**, e2020GL089316. https://doi.org/10.1029/2020GL089316

Gee, L. S., & Jordan, T. H. (1992). Generalized seismological data functionals. *Geophysical Journal International,* **111**(2), 363-390. https://doi.org/10.1111/j.1365-246x.1992.tb00584.x

Gordon, M. B., & Hempton, M. R. (1986). Collision-induced rifting: The Grenville Orogeny and the Keweenawan Rift of North America. *Tectonophysics*, **127**(1–2), 1–25. https://doi.org/10.1016/0040-1951(86)90076-4

Green, J. C. (1983). Geologic and geochemical evidence for the nature and development of the Middle Proterozoic (Keweenawan) Midcontinent Rift of North America. *Tectonophysics,* **94**, 413–437. https://doi.org/10.1016/0040-1951(83)90027-6.

Gupta, S., Mishra, S., & Rai, S. S. (2010). Magmatic underplating of crust beneath the Laccadive Island, NW Indian Ocean. *Geophysical Journal International*, **183**(2), 536-542.

Hamilton, D. A., & Mereu, R. F. (1993). 2-D Tomographic Imaging Across the North American Mid-Continent Rift System. *Geophysical Journal International,* **112**(3), 344-358. https://doi.org/10.1111/j.1365-246x.1993.tb01174.x

Halls, H. C. (1969). Compressional wave velocities of Keweenawan rock specimens from the Lake Superior region. *Can. J. Earth Sci.,* **6**, 555-568.

Hinze, W.J., Allen, D.J., Fox, A.J., Sunwood, D., Woelk, T., Green, A.G. (1992). Geophysical investigations and crustal structure of the North American Midcontinent rift system. *Tectonophysics,* **213**, 17–32.

Holm, D., Anderson, R., Boerboom, T., Cannon, W., Chandler, V., Jirsa, M., & van Schmus, W. R. (2007). Reinterpretation of Paleoproterozoic accretionary boundaries of the north-central United States based on a new aeromagnetic-geologic compilation. *Precambrian Research,* **157**(1-4), 71-79. https://doi.org/10.1016/j.precamres.2007.02.023

Hutchinson, D. R., White, R. S., Cannon, W. F., & Schulz, K. J. (1990). Keweenaw hot spot: Geophysical evidence for a 1.1 Ga mantle plume beneath the Midcontinent Rift System. *Journal of Geophysical Research,* **95**(B7), 10869-10884. https:// doi.org/10.1029/jb095ib07p10869

Hutchinson, D. R., Lee, M. W., Behrendt, J., Cannon, W. F., and Green, A. G. (1992). Variations in the reflectivity of the Moho transition zone beneath the Midcontinent Rift System of North America: Results from true amplitude analysis of GLIMPCE data. *J. Geophys. Res*., **97**(B4), 4721– 4737. doi:10.1029/91JB02572.

IRIS Transportable Array (2003). *USArray Transportable Array* [Data set]. International Federation of Digital Seismograph Networks. https://doi.org/10.7914/SN/TA

Jin, G., & Gaherty, J. B. (2015). Surface wave phase-velocity tomography based on multichannel cross-correlation. *Geophysical Journal International,* **201**(3), 1383-1398. https://doi.org/10.1093/gji/ggv079

Jirsa, M. A., Boerboom, T. J., Chandler, V. M., Mossler, J. H., A. C., & Setterholm, D. R. (2011). Geologic map of Minnesota-bedrock geology [Map]. S-22, Geologic Map of Minnesota, Precambrian Bedrock Geology. *Minnesota Geologic Survey State Map Series S-2*. Minneapolis, MN:, University of Minnesota.

Klasner, J. S., Wold, R. J., Hinze, W. J., Bacon, L. O., O'Hara, N. W. & Berkson, J. M. (1979). Bouguer gravity anomaly map of the northern Michigan-Lake Superior region, scale 1:1,000,000, *U.S. Geol. Surv. Geophys. Invest. Map*, GP-930, 1979.

Korsman, K., Korja, T., Pajunen, M., Virransalo, P., & GGT/SVEKAWorking Group (1999). The GGT/SVEKA transect: structure and evolution of the continental crust in the Palaeoproterozoic Svecofennian orogen in Finland. *International Geology Review,* **41**, 287–333.

Ligorria, J.P. & Ammon, C.J. (1999). Iterative deconvolution and receiverfunction Estimation. *Bull. seism. Soc. Am.*, **89**(5), 1395–1400.

Lin, F.-C. & Ritzwoller, M.H. (2011). Helmholtz surface wave tomography for isotropic and azimuthally anisotropic structure. *Geophys. J. Int.*, **186**(3), 1104–1120.

Lin, F., Moschetti, M. P., & Ritzwoller, M. H. (2008). Surface wave tomography of the western United States from ambient seismic noise: Rayleigh and Love wave phase velocity maps. *Geophysical Journal International,* **173**(1), 281-298. https://doi.org/10.1111/j.1365-246x.2008.03720.x

Lippus, C. S. (1988). The seismic properties of mafic volcanic rocks of the Keweenawan Supergroup and their implications, M. Sc. thesis, 118 pp., Purdue Univ., West Lafayette, Indiana.

Marzen, R. E., Shillington, D. J., Lizarralde, D., & Harder, S. H. (2019). Constraints on Appalachian orogenesis and continental rifting in the southeastern United States from wide-angle seismic data. *Journal of Geophysical Research: Solid Earth*, **124**, 6625–6652. https://doi.org/10.1029/2019JB017611

Mengel, K., & Kern, H. (1992). Evolution of the petrological and seismic Moho; implications for the continental crust–mantle boundary. *Terra Nova,* **4**, 109–116.

Merino, M., Keller, G. R., Stein, S., & Stein, C. (2013). Variations in Mid-Continent Rift magma volumes consistent with microplate evolution. *Geophysical Research Letters,* **40**(8), 1513-1516. https://doi.org/10.1002/grl.50295

Middleton, R. S., Borradaile, G. J., Baker, D., & Lucas, K. (2004). Proterozoic diabase sills of northern Ontario: Magnetic properties and history. *Journal of Geophysical Research: Solid Earth,* **109**(B2). https://doi.org/10.1029/2003jb002581

Miller, J. D., & Nicholson, S. W. (2013). Geology and mineral deposits of the 1.1 Ga Mid-continent Rift in the Lake Superior region—An overview (J. D. Miller, Ed.). In *Field Guide to the Cu-Ni-PGE Deposits of the Lake Superior Region* (Precambrian Research Center Guidebook 13-1, pp. 1-50). Duluth, MN: University of Minnesota Press.

Moidaki, M., Gao, S. S., Liu, K. H., & Atekwana, E. (2013). Crustal thickness and Moho sharpness beneath the Midcontinent rift from receiver functions. *Research in Geophysics,* **3**(1), 1-7. https://doi.org/10.4081/rg.2013.e1

Morgan, W. J. (1971). Convection Plumes in the Lower Mantle. *Nature,* **230**(5288), 42-43. doi:10.1038/230042a0

Moschetti, M. P., Ritzwoller, M. H., Lin, F., & Yang, Y. (2010). Crustal shear wave velocity structure of the western United States inferred from ambient seismic noise and earthquake data. *Journal of Geophysical Research,* **115**(B10). https://doi.org/10.1029/2010jb007448

Nicholson, S. W., & Shirey, S. B. (1990). Midcontinent rift volcanism in the Lake Superior Region: Sr, Nd, and Pb isotopic evidence for a mantle plume origin. *Journal of Geophysical Research,* **95**(B7), 10851-10868. https://doi.org/10.1029/jb095ib07p10851

Nicholson, S. W., Schulz, K. J., Shirey, S. B., & Green, J. C. (1997). Rift-wide correlation of 1.1 Ga Midcontinent rift system basalts: implications for multiple mantle sources during rift development. *Canadian Journal of Earth Sciences,* **34**(4), 504-520. https://doi.org/10.1139/e17-041

Ojakangas, R., Morey, G., & Southwick, D. (2001). Paleoproterozoic basin development and sedimentation in the Lake Superior region, North America. *Sedimentary Geology, 141-142*, 319-341. doi:10.1016/s0037-0738(01)00081-1

Ola, O., Frederiksen, A. W., Bollmann, T., van der Lee, S., Darbyshire, F. A., Wolin, E., Revenaugh, J., Stein, C., Stein, S., & Wysession, M. E. (2016). Anisotropic zonation in the lithosphere of Central North America: Influence on the Mid-Continent Rift, *Tectonophysics*, **683***(30),* 367-381. doi: 10.1016/j.tecto.2016.06.031.

Olugboji, T. M., & Park, J. (2016). Crustal anisotropy beneath Pacific Ocean-Islands from harmonic decomposition of receiver functions. *Geochem. Geophys. Geosyst.*, **17**, 810– 832. doi:10.1002/2015GC006166.

Percival, J.A., Skulski, T., Sanborn-Barrie, M., Stott, G.M., Leclair, A.D., Corkery, M.T., & Boily, M. (2012). Geology and tectonic evolution of the Superior Province, Canada. Chapter 6 *In* Tectonic Styles in Canada: The LITHOPROBE Perspective. J.A. Percival, F.A. Cook, and R.M. Clowes (Eds). Geological Association of Canada, (Special Paper 49, pp. 321–378).

Pollitz, F. F., & Mooney, W. D. (2016). Seismic velocity structure of the crust and shallow mantle of the Central and Eastern United States by seismic surface wave imaging. *Geophysical Research Letters,* **43**(1), 118-126. https://doi.org/10.1002/2015gl066637

Prasanna M., Moucha, R., Rooney, T., Stein, S., & Stein, C. (2022). North America's Midcontinent Rift magma volume: A coincidental rendezvous of a plume with a rift. *Geology*, **50**(10), 1125-1129. doi: https://doi.org/10.1130/G49913.1.

Rooney, T., Konter, J., Finlayson, V., LaVigne, A., Brown, E., Stein, C., Stein, S., and Moucha, R. (2022). Constraining the isotopic endmembers contributing to 1.1 Ga Keweenawan large igneous province magmatism. *Contributions to Mineralogy and Petrology*, **177**, 49, https://doi.org/10.1007/s00410-022-01907-8.

Rivers, T. (2015). Tectonic setting and evolution of the Grenville orogen: an assessment of progress over the last 40 years. *Geosci. Can*., **42**, 77–123. https://doi.org/10.12789/geocanj.2014.41.057.

Rudnick, R. L., & Fountain, D. M. (1995). Nature and composition of the continental crust: A lower crustal perspective. *Reviews of Geophysics,* **33**(3), 267. https://doi.org/10.1029/95rg01302

Schmandt, B., Lin, F. C., & Karlstrom, K. E. (2015). Distinct crustal isostasy trends east and west of the Rocky Mountain Front. *Geophysical Research Letters*, **42**, 10,290–10,298.

Schulte-Pelkum, V., Mahan, K. H., Shen, W., & Stachnik, J. C. (2017), The distribution and composition of high velocity lower crust across the continental U.S.: Comparison of seismic and xenolith data and implications for lithospheric dynamics and history. *Tectonics*, **36**, 1455–1496. doi: 10.1002/2017TC004480.

Schultz, C.A., Myers, S.C., Hipp, J. & Young, C.J. (1999). Nonstationary Bayesian kriging: a predictive technique to generate spatial corrections for seismic detection, location and identification. *Phys. Earth planet. Inter*., **113**, 321–338.

Schulz, K. J., & Cannon, W. F. (2007). The Penokean orogeny in the Lake Superior region. *Precambrian Research,* **157**(1-4), 4-25. https://doi.org/10.1016/j.precamres.2007.02.022

Shay, J., & Tréhu, A. (1993). Crustal structure of the central graben of the Midcontinent Rift beneath Lake Superior. *Tectonophysics,* **225**(4), 301-335. https://doi.org/10.1016/0040-1951(93)90303-2

Shen, W., & Ritzwoller, M. H. (2016), Crustal and uppermost mantle structure beneath the United States. *J. Geophys. Res.: Solid Earth*, **121**, 4306– 4342. doi:10.1002/2016JB012887

Shen, W., Ritzwoller, M. H., Schulte-Pelkum, V., & Lin, F. (2013a). Joint inversion of surface wave dispersion and receiver functions: a Bayesian Monte-Carlo approach. *Geophysical Journal International,* **192**(2), 807-836. https://doi.org/10.1093/gji/ggs050

Shen, W., Ritzwoller, M. H., & Schulte-Pelkum, V. (2013b). A 3-D model of the crust and uppermost mantle beneath the Central and Western US by joint inversion of receiver functions and surface wave dispersion. *J. of Geophys. Res.: Solid Earth,* **118**(1), 262-276. https://doi.org/10.1029/2012jb009602

Shen, W., Ritzwoller, M. H., & Schulte-Pelkum, V. (2013c). Crustal and uppermost mantle structure in the central US encompassing the Midcontinent Rift. *J. of Geophys. Res.*: *Solid Earth,* **118**(8), 4325-4344.

Shen, W., Wiens, D. A., Anandakrishnan, S., Aster, R. C., Gerstoft, P., Bromirski, P. D., Hansen, S. E., Dalziel, I. A. D., Heeszel, D. S., Huerta, A. D., Nyblade, A. A., Stephen, R., Wilson, T. J., & Winberry, J. P. (2018). The crust and upper mantle structure of central and West Antarctica from Bayesian inversion of Rayleigh wave and receiver functions. *Journal of Geophysical Research: Solid Earth*, **123**, 7824– 7849. https://doi.org/10.1029/2017JB015346

Shirey, S. B., Klewin, K. W., Berg, J. H., & Carlson, R. W. (1994). Temporal changes in the sources of flood basalts: Isotopic and trace element evidence from the 1100 Ma old Keweenawan Mamainse Point Formation, Ontario, Canada. *Geochimica et Cosmochimica Acta,* **58**(20), 4475-4490. https://doi.org/10.1016/0016-7037(94)90349-2

Sims, P. K., van Schmus, W. R., Schulz, K. J., & Peterman, Z. E. (1989). Tectono-stratigraphic evolution of the Early Proterozoic Wisconsin magmatic terranes of the Penokean Orogen. *Canadian Journal of Earth Sciences,* **26**(10), 2145-2158. https://doi.org/10.1139/e89-180

Stein, C. A., Stein, S., Merino, M., Randy Keller, G., Flesch, L. M., & Jurdy, D. M. (2014). Was the Midcontinent Rift part of a successful seafloor-spreading episode? *Geophysical Research Letters*, **41**, 1465-1470. https://doi.org/10.1002/2013GL059176

Stein, C.A., Kley, J., Stein, S., Hindle, D., & Keller, G. R. (2015). North America's Midcontinent Rift: When rift met LIP. *Geosphere*, **11**(5), 1607-1616. doi:10.1130/GES01183.1.

Stein, S., van der Lee, S., Jurdy, D., Stein, C., Wiens, D. A., Wysession, M. E., Revenaugh, J., Frederiksen, A., Darbyshire, F., Bollmann, T., Lodewyk, J., Wolin, E., Merino, M., & Tekverk, K**.** (**2011).** Learning from failure: The SPREE Mid-Continent Rift Experiment. *GSA Today,* **21**(9), 5-7. https://doi.org/10.1130/g120a.1

Stein, S., Brown, E., Darbyshire, F., Frederiksen, A., Jurdy, D., Kley, J., Moucha, R., Stein, C. A., Rooney, T., Wiens, D. A., & Wysession, M. E. (2016). New Insights into North America's Midcontinent Rift. *Eos,* **97**. https://doi.org/10.1029/2016eo056659

Stein, S., Stein, C., Elling R., Kley, J., Keller, R., Wysession, M. E., Rooney T., Frederiksen, A., & Moucha, R. (2018), Insights from North America's Failed Midcontinent Rift into the Evolution of Continental Rifts and Passive Continental Margins. *Tectonophysics,* **744***,* 403-421. https://doi.org/10.1016/j.tecto.2018.07.021.

Swanson-Hysell, N. L., Rivers, T. & van der Lee, S. (2023). The late Mesoproterozoic to early Neoproterozoic Grenvillian orogeny and the assembly of Rodinia: Turning point in the tectonic evolution of Laurentia. In the GSA Memoir entitled*: Laurentia: Evolution of a Continent*, in press.

Thomas, M. D., & Teskey, D. J. (1994). An interpretation of gravity anomalies over the Midcontinent Rift, Lake Superior, constrained by GLIMPCE seismic and aeromagnetic data. *Canadian Journal of Earth Sciences,* **31**(4), 682-697. https://doi.org/10.1139/e94-061

Thybo, H., & Artemieva, I. M. (2013). Moho and magmatic underplating in continental lithosphere. *Tectonophysics*, **609**, 605–619. doi:10.1016/j.tecto.2013.1005.1032.

Thybo, H., Janik, T., Omelchenko, V.D., et al. (2003). Upper lithospheric seismic velocity structure across the Pripyat Trough and the Ukrainian Shield along the EUROBRIDGE'97 profile. *Tectonophysics,* **371**, 41–79.

Tian, H., & He, C. (2021). Vestiges of underplating and assembly in the central North China Craton based on S-wave velocities. *Sci Rep*, **11**, 21218. https://doi.org/10.1038/s41598-021-00756-y

Tréhu, A., Morel-à-l'Huissier, P., Meyer, R., Hajnal, Z., Karl, J., Mereu, R., Sexton, J., et al. (1991). Imaging the Midcontinent Rift beneath Lake Superior using large aperture seismic data. *Geophysical Research Letters,* **18**(4), 625-628.

Van der Lee, S., Wiens, D., Revenaugh, J., Frederiksen, A., & Darbyshire, F. (2011). *Superior Province Rifting EarthScope Experiment* [Data set]. International Federation of Digital Seismograph Networks. https://doi.org/10.7914/SN/XI_2011

Van der Meijde, M., Van der Lee, S., & and Giardini, D. (2003). Crustal structure beneath broad-band seismic stations in the Mediterranean region. *Geophys. J. Int*., **152**(3), 729–739.

Van der Pluijm, V. D., & Marshak, S. (2004). *Earth structure: an introduction to structural geology and tectonics*. New York: W.W. Norton.

Van Schmus, W. R. (1992). Tectonic setting of the Midcontinent Rift system. *Tectonophysics*, **213**(1-2), 1-15.

Van Schmus, W. R., Bickford, M. E., & Zietz, I. (1987). Early and Middle Proterozoic provinces in the central United States (A. Kroner, Ed.). *Proterozoic Lithospheric Evolution* (Ser. 17, pp. 43-68). *American Geophysical Union Geodynamics Series*.

Van Schmus, W. R., & Hinze, W. J. (1985). The Midcontinent Rift System. *Annual Review of Earth and Planetary Sciences,* **13**(1), 345-383. https://doi.org/10.1146/annurev.earth.13.1.345

Vervoort, J. D., Wirth, K., Kennedy, B., Sandland, T., & Harpp, K. S. (2007). The magmatic evolution of the Midcontinent rift: New geochronologic and geochemical evidence from felsic magmatism. *Precambrian Research,* **157**(1-4), 235-268. https://doi.org/10.1016/j.precamres.2007.02.019

Wessel, P., Smith, W. H., Scharroo, R., Luis, J., & Wobbe, F. (2013). Generic Mapping Tools: Improved Version Released. *Eos, Transactions American Geophysical Union,* **94**(45), 409-410. https://doi.org10.1002/2013eo450001

White, R. S. (1997). Mantle temperature and lithospheric thinning beneath the Midcontinent rift system: evidence from magmatism and subsidence. *Canadian Journal of Earth Sciences,* **34**(4), 464-475. https://doi.org/10.1139/e17-038

White, R. S., & McKenzie, D. P. (1989). Magmatism at rift zones: The generation of volcanic continental margins and flood basalts*, J. Geophys. Res*., **94**, 7685-7729.

Whitmeyer, S.J., Karlstrom, K.E. (2007). Tectonic model for the Proterozoic growth of North America. *Geosphere,* **3**, 220–259. https://doi.org/10.1130/GES00055.1

Wielandt, E. (1993). Propagation and structural interpretation of non-plane waves. *Geophys. J. Int*., **113**(1), 45–53.

Wolin, E., van der Lee, S., Bollmann, T. A., Wiens, D. A., Revenaugh, J., Darbyshire, F. A., Frederiksen, A. W., Stein, S., & Wysession, M. E. (2015). Seasonal and diurnal variations in long-period noise at SPREE stations: the influence of soil characteristics on shallow stations' performance. *Bull. Seismol. Soc. Am*., **105**, 2433-2452, doi:10.1785/0120150046

Wysession, M. E., & Fischer, K. M. (2001). The Florida to Edmonton Broadband Experiment. International Federation of Digital Seismograph Networks. Other/Seismic Network, https://doi.org/10.7914/SN/XR_2001

Yang, B., Egbert, G. D., Kelbert, A., & Meqbel, N. M. (2015). Three-dimensional electrical resistivity of the north-central USA from EarthScope long period magnetotelluric data. *Earth and Planetary Science Letters,* **422**, 87-93. https://doi.org/10.1016/j.epsl.2015.04.006

Yang, Y., Ritzwoller, M. H., Levshin, A. L., & Shapiro, N. M. (2007). Ambient noise Rayleigh wave tomography across Europe. *Geophysical Journal International,* **168**(1), 259-274. https://doi.org/10.1111/j.1365-246x.2006.03203.x

Zhang, H., Lee, S. V., Wolin, E., Bollmann, T. A., Revenaugh, J., Wiens, D. A., Frederiksen, A. W., Darbyshire, F. A., Aleqabi, G. I., Wysession M. E., Stein, S., & Jurdy, D. M. (2016). Distinct crustal structure of the North American Midcontinent Rift from P wave receiver functions. *Journal of Geophysical Research: Solid Earth,* **121**(11), 8136-8153. https://doi.org/10.1002/2016jb013244

Zhu, L., and Kanamori, H. (2000). Moho depth variation in southern California from teleseismic receiver functions. *J. Geophys. Res*., **105**(B2), 2969–2980.